





RESEARCH ARTICLE

10.1002/2017JE005371

A Geophysical Perspective on the Bulk Composition of Mars

A. Khan¹ , C. Liebske², A. Rozel¹, A. Rivoldini³, F. Nimmo⁴ , J. A. D. Connolly² , A.-C. Plesa⁵ , and D. Giardini¹

Key Points:

- We constrain the bulk composition of Mars using geophysical data to an Fe/Si (wt) of 1.61 ± 0.167 and a molar Mg# of 0.745–0.751
- The results indicate a large liquid core (1,640–1,740 km in radius) containing 13.5–16 wt% S and excludes a transition to a lower mantle
- We use the inversion results in tandem with geodynamic simulations to identify plausible geodynamic scenarios and parameters

Supporting Information:

- Supporting Information S1

Correspondence to:

A. Khan,
amir.khan@erdw.ethz.ch

Citation:

Khan, A., Liebske, C., Rozel, A., Rivoldini, A., Nimmo, F., Connolly, J. A. D., ... Giardini, D. (2018). A geophysical perspective on the bulk composition of Mars. *Journal of Geophysical Research: Planets*, 123, 575–611. <https://doi.org/10.1002/2017JE005371>

Received 5 JUL 2017

Accepted 31 AUG 2017

Accepted article online 14 NOV 2017

Published online 26 FEB 2018

¹Institute of Geophysics, ETH Zürich, Zurich, Switzerland, ²Institute of Geochemistry and Petrology, ETH Zürich, Zurich, Switzerland, ³Royal Observatory of Belgium, Brussels, Belgium, ⁴Department of Earth and Planetary Sciences, University of California, Santa Cruz, CA, USA, ⁵German Aerospace Center (DLR), Berlin, Germany

Abstract We invert the Martian tidal response and mean mass and moment of inertia for chemical composition, thermal state, and interior structure. The inversion combines phase equilibrium computations with a laboratory-based viscoelastic dissipation model. The rheological model, which is based on measurements of anhydrous and melt-free olivine, is both temperature and grain size sensitive and imposes strong constraints on interior structure. The **bottom of the lithosphere, defined as the location where the conductive geotherm meets the mantle adiabat, occurs deep within the upper mantle (~200–400 km depth) resulting in apparent upper mantle low-velocity zones.** Assuming an Fe-FeS core, our results indicate **(1) a mantle with a Mg# (molar Mg/Mg+Fe) of ~0.75** in agreement with earlier geochemical estimates based on analysis of Martian meteorites; **(2) absence of bridgmanite-** and ferropericlase-dominated basal layer; **(3) core compositions (15–18.5 wt% S),** core radii (1,730–1,840 km), and core-mantle boundary temperatures (1620–1690°C) that, together with the **eutectic-like core compositions, suggest that the core is liquid;** and (4) bulk Martian compositions with a Fe/Si (weight ratio) of 1.66–1.81. We show that the inversion results can be used in tandem with geodynamic simulations to identify plausible geodynamic scenarios and parameters. Specifically, we find that the inversion results are largely reproducible by stagnant lid convection models for a range of initial viscosities (~10¹⁸–10²⁰ Pa s) and radioactive element partitioning between crust and mantle around 0.01–0.1. The geodynamic models predict a mean surface heat flow between 15 and 25 mW/m².

1. Introduction

Knowledge of the internal constitution of the planets is crucial to our understanding of the origin and evolution of the solar system. Major constraints can be placed on planetary accretion, differentiation, and mantle evolution from knowledge of bulk chemical composition (e.g., Taylor, 1999). By far the largest insights into the physical structure of the Earth have come from geophysical analyses, and seismology in particular. However, the dearth of geophysical data pertinent to the interior of other planets has made this approach less instructive and a significant part of current knowledge on mantle and bulk composition of the terrestrial planets derives from geochemical/cosmochemical and isotopic analyses of rocks and primitive solar system material (e.g., Drake & Richter, 2002; Palme & O'Neill, 2003; Richter et al., 2006; Ringwood, 1979; Taylor, 1980; Taylor et al., 2006).

For Mars, an increasing amount of observations, both in situ and from laboratory analyses of Martian meteorites and cosmochemical material, have become available (e.g., Norman, 1999; Taylor, 2013). Geodetic data in the form of Doppler observations obtained from ranging to orbiting and landed spacecraft (Viking, Mars Pathfinder, Mars Global Surveyor, Mars Odyssey, and Mars Reconnaissance Orbiter) over more than a decade resulted in the recognition that Mars has a relatively thick crust (average thickness of 50 km) and an Fe-rich possibly liquid core (e.g., Bills et al., 2005; Folkner et al., 1997; Genova et al., 2016; Konopliv et al., 2006, 2011, 2016; Lainey et al., 2007; Neumann et al., 2004; Yoder et al., 2003). In addition, data and results from geophysical modeling and mantle convection studies that bear on interior structure (e.g., Baratoux et al., 2014; Elkins-Tanton et al., 2003; Grott & Breuer, 2008; Hauck & Phillips, 2002; Khan & Connolly, 2008; Kiefer & Li, 2009; Mocquet et al., 2011, 1996; Neumann et al., 2004; Plesa et al., 2015; Rai & Westrenen, 2013; Rivoldini et al., 2011; Ruedas et al., 2013a; Sohl & Spohn, 1997; Verhoeven et al., 2005; Wiczeorek & Zuber, 2004; Williams & Nimmo, 2004; Yoder et al., 2003) have allowed us to refine our understanding of planetary processes from a Martian vantage point; yet much remains to be understood. Among others, how well do we really know the composition of Mars

and its core size and state, and how can current estimates be improved? Does Mars contain the terrestrial equivalent of a lower mantle layer, and what is its role in the evolution of the core?

The aim of this study is to reassess and possibly improve current constraints on Mars's bulk composition and thermal state from inversion of the available geophysical data (mean mass and moment of inertia, global tidal dissipation, and magnitude of tidal response). To this end we will build upon our previous work (e.g., Khan et al., 2007) to (1) invert different geophysical data sets directly for compositional and thermal parameters and combine this with (2) a method for computing tidal dissipation within a planet using the laboratory-based grain size- and frequency-dependent viscoelastic model of Jackson and Faul (2010). The main point is to link the dissipation model, which is based on laboratory experiments on anhydrous melt-free polycrystalline olivine, with thermodynamic phase equilibrium computations in order to self-consistently compute geophysical responses that can be compared directly to observations. This approach has a number of advantages: (1) It anchors temperature, composition, dissipation, and discontinuities that are in laboratory-based forward models; (2) it permits the simultaneous use of geophysical inverse methods to optimize profiles of physical properties (e.g., shear modulus, dissipation, and density) to match geophysical data; and (3) it is capable of making quantitative predictions that can be tested with the upcoming Mars InSight mission to be launched in May 2018 (Banerdt et al., 2013) (InSight will emplace a seismometer, a heat flow probe, and a geodetic experiment on Mars) and/or tested against results and data from other studies (e.g., geodynamical simulations of planet evolution, petrological analyses of Martian meteorites, and orbit-imaged surface chemistry and crustal thickness).

As a means of illustrating these points, we show that the inversion results can be used in combination with geodynamic simulations to identify plausible geodynamic scenarios and parameters. This coupling of geodynamics and geophysics (e.g., Dannberg et al., 2017) has the advantage that it anchors geodynamic models in geophysically constrained results. These simulations, based on the StagYY code (Tackley, 2008), explicitly consider grain size evolution and suggest that stagnant lid convection is capable of explaining the various observables (crustal and lithospheric thickness and present-day grain size and mantle temperatures) assuming reasonable initial estimates of viscosity, radioactive element partitioning, and initial temperature field. The models are also able to predict the present-day mean surface heat flow, which can be compared to surface observations to be made with InSight (e.g., Plesa et al., 2016).

In the following we discuss constraints that derive from geochemical and cosmochemical analyses and summarize previous geophysical analyses that bear on the interior of Mars (section 2); enumerate the geophysical data employed in the present analysis and detail the computation of crust, mantle, and core properties (section 3) and numerical modeling aspects of solving the forward and inverse problem posited here (section 4); and, finally, describe and discuss results.

2. Background

2.1. Geochemical Perspective

Our knowledge on the chemistry of the Martian mantle and core originates to a large extent from the chemical and isotopic compositions of a class of basaltic meteorites that are believed to be fragments ejected from the Martian surface on meteoritic impacts and collectively known as SNC meteorites (Shergottites, Nahklites, and Chassignites) (e.g., McSween, 1985, 1994), hereinafter referred to as Martian meteorites. A key argument for this hypothesis is the concentration of entrapped gases within shergottite meteorites that match the values measured for the Martian atmosphere by the Viking mission (Bogard et al., 2001). The Martian meteorites also exhibit relatively young crystallization ages (Stolper & McSween, 1979). Shergottites have ages in the range of 170–600 Ma (McSween & McLennan, 2014, and references therein), which require a sufficiently large planet as parent body because it is physically implausible, due to thermal constraints, to maintain magmatic activity on asteroid-sized bodies so late in the solar systems history.

Different lines of arguments have been used to derive the chemical composition of the Martian mantle and core from the chemical compositions of the Martian meteorites. These can be categorized in two general groups that consider (1) the abundance of refractory elements in the Martian meteorites (Dreibus & Wänke, 1984, 1985; Halliday et al., 2001; Longhi et al., 1992; Taylor, 2013) and (2) oxygen isotope systematics (Burbine & O'Brien, 2004; Lodders & Fegley, 1997; Sanloup et al., 1999). Common to both approaches is the notion that Mars is considered to have accreted from different material which condensed from the solar nebular, including highly volatile-depleted and reduced components and oxidized, volatile-rich condensates.

Exemplary of the first line of arguments was the approach of Dreibus and Wänke (hereafter DW model) (Dreibus & Wänke, 1984, 1985, 1987). The DW model has become the standard model for Mars and has served as reference in many subsequent studies (e.g., Bertka & Fei, 1997; Bertka & Holloway, 1994; Collinet et al., 2015; Matsukage et al., 2013). The essence of this model lies in the assumption that Mars accreted heterogeneously from two different cosmochemical reservoirs, that is, a highly reduced component during the early stages, followed by the addition of oxidized, volatile-rich material during the final stages of accretion. The reduced component is assumed to have CI-chondritic element abundances that are more refractory than Mn, that is, elements having higher condensation temperatures than this element, whereas the late stage oxidized component is entirely CI-chondritic. Thus, a central tenet inherent of the DW model is that refractory elements follow CI-chondritic proportions. Chemical analyses of the Martian meteorites known at that time indicated that their Mn content is close to CI-chondritic; thus, this element became key to the bulk chemical composition of Mars. To derive the composition of the mantle, fractionation trends that occur during igneous processes are invoked, which allow conclusions about the Shergottites source region to be drawn. Recently, Taylor (2013) reassessed the primitive mantle composition with a similar strategy as DW using a much larger meteoritic record (~60 versus 6). For the elements of interest here (major and minor but no trace elements), the Taylor bulk silicate Mars model is almost identical in terms of elemental concentrations to that of DW. However, there is considerable difference in the assumption of the S content of the planet. In the model of Taylor (2013), the core is significantly more S-rich compared to DW.

Morgan and Anders (1979) derived a chemical composition using a similar methodology as DW, that is, to scale the concentration of “unknown” to “known” elements (or known elemental ratios) based on volatility trends. It should be noted that Morgan and Anders (1979) developed their model before the general acceptance that Martian meteorites originated from Mars and, for example, their known K/U ratio was taken from the Soviet orbiter Mars 5 mission (Surkov, 1977) with several corrections applied based on various assumptions. As pointed out by Taylor et al. (2006), the value of K/U and K/Th as a proxy for the proportions of moderately volatile versus refractory elements was later corrected. This likely explains some systematic differences between the Morgan and Anders composition and other estimates.

As an illustration of the second approach to derive the Martian bulk composition is to consider the oxygen isotopic systematics of the Martian meteorites (e.g., Lodders & Fegley, 1997; Mohapatra & Murty, 2003; Sanloup et al., 1999). Oxygen is by far the most abundant element in the silicate proportions of the terrestrial planets, and the Martian meteorites form a fractionation line in a $\delta^{17}\text{O}/\delta^{18}\text{O}$ three-isotope plot which is distinctively different from terrestrial or other meteoritic trends. The aforementioned two studies are based on the assumptions that Mars is the parent body of the Martian meteorites and that their isotopic compositions can be described by mixing different classes of meteorites. Based on this, the oxygen isotope composition of Mars is deduced from mass balancing various meteoritic end-members. The concentrations of all other elements are then simply defined by the chemical composition and mass fraction of the various meteorite end-member components. Core and silicate mantle compositions are finally deduced from the total oxygen content and redox equilibria, which leaves a proportion of Fe and the majority of Ni and S in the metallic core.

The differences in the models of Lodders and Fegley (1997) and Sanloup et al. (1999) are determined by the choices of end-member components (meteorite classes) but generally lead to comparable results for major and minor elements. Lodders and Fegley (1997) invoked three end-members: (1) mean values of reduced and volatile-depleted H- (ordinary) chondrites; (2) moderately oxidized CV-chondrites; and (3) highly oxidized and volatile-rich CI-chondrites. These end-members span a compositional triangle in the three-isotope $\delta^{17}\text{O}/\delta^{18}\text{O}$ diagram around the Martian meteorites. The model of Sanloup et al. (1999) (EH45:H55) is based on a mixture of two end-members, a mean value of highly reduced EH- (enstatite) chondrites (45%) and a hypothetical but as yet unsampled H- (ordinary) chondrite component (55%) that is located on an isotopic fractionation line along with LL-, L-, and H-chondrites. This hypothetical end-member is required to produce a mixing line with the EH-chondrite component that passes through the Martian meteorite oxygen isotope mean value.

2.2. Summary of Geochemical Models

To investigate the effect of varying bulk chemical compositions of Mars, we have selected the five possible bulk compositions discussed above. We consider the compositions proposed by (1) Dreibus and Wänke (1984) and (2) Taylor (2013) as representative of the CI refractory element approach but with different core Fe/S ratios;

Table 1
 Model Martian Compositions

	Morgan and Anders (1979) (MA)	Dreibus and Wänke (1984) (DW)	Lodders and Fegley (1997) (LF)	Sanloup (1999) (SAN)	Taylor (2013) (TAY)
Mantle composition					
SiO ₂	41.59	44.47	45.39	47.79	43.70
Al ₂ O ₃	6.39	2.94	2.89	2.52	3.04
MgO	29.77	30.16	29.71	27.46	30.50
CaO	5.16	2.43	2.36	2.01	2.43
Na ₂ O	0.10	0.51	0.98	1.21	0.53
K ₂ O	0.01	0.04	0.11	—	0.04
TiO ₂	0.33	0.13	0.14	0.10	0.14
Cr ₂ O ₃	0.65	0.77	0.68	0.70	0.73
MnO	0.15	0.51	0.37	0.40	0.44
FeO	15.85	17.89	17.21	17.81	18.10
P ₂ O ₅	—	0.17	0.18	—	0.15
Core composition					
Fe	88.1	77.8	81.1	76.6	78.6 ^a
Co	0.4	0.4	0.4	0.0	
Ni	8.0	7.6	7.7	7.2	
S	3.5	14.2	10.6	16.2	21.4
P	0.0	0.0	0.2	0.0	
Model mantle composition					
SiO ₂	42.0	44.8	45.7	48.0	44.1
Al ₂ O ₃	6.9	3.5	3.4	3.0	3.5
MgO	29.9	30.3	29.8	27.5	30.7
CaO	5.2	2.4	2.4	2.0	2.4
FeO	16.0	18.5	17.6	18.3	18.7
Na ₂ O	0.1	0.5	1.1	1.2	0.6
Model core composition					
Fe	96	86	89	84	79
S	4	14	11	16	21
Average crustal composition					
SiO ₂	50.7				
Al ₂ O ₃	10.9				
MgO	9.2				
CaO	7.0				
FeO	18.8				
Na ₂ O	3.3				

Note. The average crustal composition is that of Taylor and McLennan (2009) assuming a mass fraction of 0.5, which corresponds to a crustal thickness of 50 km. The average crustal composition applies to all mantle models.

^aTaylor (2013) assumes a core composition of Fe + Ni. Molar proportions of other minor oxide components were added to the major components according to valence and chemical behavior of the cations; for example, the molar amounts of Cr₂O₃ and MnO were added to Al₂O₃ and FeO, respectively, whereas we ignored P₂O₅. For the core system the molar proportions of Ni and Co were replaced by Fe. All numbers in weight percent.

(3) the compositions of Lodders and Fegley (1997) and (4) Sanloup (1999) (EH45:H55) as representative of the oxygen isotope approach; and (5) the composition of Morgan and Anders (1979) despite the fact that some of the key elemental ratios in that model have been revised. Nevertheless, this model is distinctively different in core composition by being significantly depleted in S by a factor of 3 to 5 compared to other models. Table 1 summarizes the five model compositions. To facilitate treatment, some simplifications to the proposed mantle

and core compositions are made; the mantle is considered as a six-component system (CaO, FeO, MgO, Al₂O₃, SiO₂, and Na₂O) to be compatible with the thermodynamic database (section 3.3), and the core system (section 3.5) is reduced to a simple Fe-S binary.

Differences in the modified bulk silicate Mars compositions (Table 1) become apparent when considering elemental ratios such as Mg/Si (molar). Mg/Si ranges from 1.07 (near CI-chondritic) to 0.86 between the studies of Morgan and Anders (1979) and Sanloup et al. (1999). These latter studies also show the widest spread in Mg number (molar Mg/Mg+Fe), which ranges from 0.77 to 0.73. Mg/Si affects the proportions of olivine (and its polymorphs) and pyroxenes (and garnet), thereby influencing the properties of the mantle. Very similar results in terms of major element ratios are observed for the models of Dreibus and Wänke (1984) and Lodders and Fegley (1997). The oxygen isotope mass balance method predicts higher alkali concentration, but this is unlikely to influence calculated mantle phase proportions. In regard to trace and volatile elements, differences between the five models are more pronounced. From a geophysical point of view, however, these differences are insignificant. We should note that the model compositions shown in Table 1 are input values only; that is, mantle and core composition are parameters to be determined in the inversion. This will be described in more detail below.

Finally, Borg and Draper (2003) and Agee and Draper (2004) have suggested that the Martian mantle may have a higher Mg# than the range of compositions described above. However, an alternative bulk Mars composition, reporting elemental concentrations for the core and a high Mg#, that is, low-FeO, bearing mantle has, to our knowledge, yet to be formulated. The possibility also exists that FeO is not homogeneously distributed throughout the mantle, as indicated by systematic differences in the surface distribution of Fe detected by the gamma ray spectrometer on board Mars Odessey (Taylor et al., 2006). The questions whether alternative bulk Mars and potentially low-FeO mantle models would satisfy the physical properties of Mars and whether the mantle is heterogeneous with regard to the distribution of major elements are beyond the scope of this paper.

2.3. Geophysical Perspective

Geophysical analyses have, for the most part, relied on results obtained from geochemical-cosmochemical studies with the purpose of predicting the geophysical response of these chemically derived models. Geophysical and experimental approaches are to a large extent based on the DW model composition with the goal of determining mantle mineralogy and density. Combined with equation-of-state (EOS) modeling this allows for determination of a model density profile for the purpose of making geophysical predictions that can be subsequently compared to observations. The studies by Bertka and Fei (1997, 1998) represent the experimental approach, while numerical approaches with varying degree of sophistication (forward/inverse modeling, number of geophysical observations, and parameterized phase diagram/phase-equilibrium computations) are embodied in the studies of Khan and Connolly (2008), Kuskov and Panferov (1993), Longhi et al. (1992), Mocquet et al. (1996), Rivoldini et al. (2011), Sohl and Spohn (1997), Sohl et al. (2005), Verhoeven et al. (2005), Wang et al. (2013), and Zharkov and Gudkova (2005). Based on the available geophysical data at the time (principally the moment of inertia), Bertka and Fei (1998), for example, concluded that the CI chondrite accretion model for deriving Mars is incompatible with a DW-like mantle composition.

According to the DW model there is evidence for chalcophile element depletion in the Martian meteorites, which suggests that the otherwise Fe-Ni-rich core contains a substantial amount of a sulfide component (S need not be the only alloying element; Zharkov and Gudkova (2005), for example, considered H in addition to S in the core). This observation is important because an alloying element acts to influence the physical state while simultaneously providing information on core temperature. In this context, there is strong evidence from measurements of the deformation of the planet due to solar tides that Mars's core or parts of it are currently liquid (Genova et al., 2016; Konopliv et al., 2016; Yoder et al., 2003) as had been predicted earlier (Lognonné & Mosser, 1993; Zharkov & Gudkova, 1997). Recent experimental studies of phase relations in the Fe-S and (Fe,Ni)-S systems at pressure and temperature conditions relevant for the core of Mars (1927°C and 40 GPa) also point to an entirely liquid core at present (Rivoldini et al., 2011; Stewart et al., 2007). Core size, state, and composition are uncertain with current estimates in the range 1,550–1,800 km in radius, 5.9–7.5 g/cm³ in density, and 64–90 wt% FeNi and 10–36 wt% S in composition (cf. Table 5 in Khan & Connolly, 2008; but see also Rivoldini et al., 2011).

Another important issue directly related to core size is the presence or absence of a lower mantle in Mars, that is, a mantle dominated by bridgmanite structure silicates. Figure 1 shows that at pressures above ~23 GPa

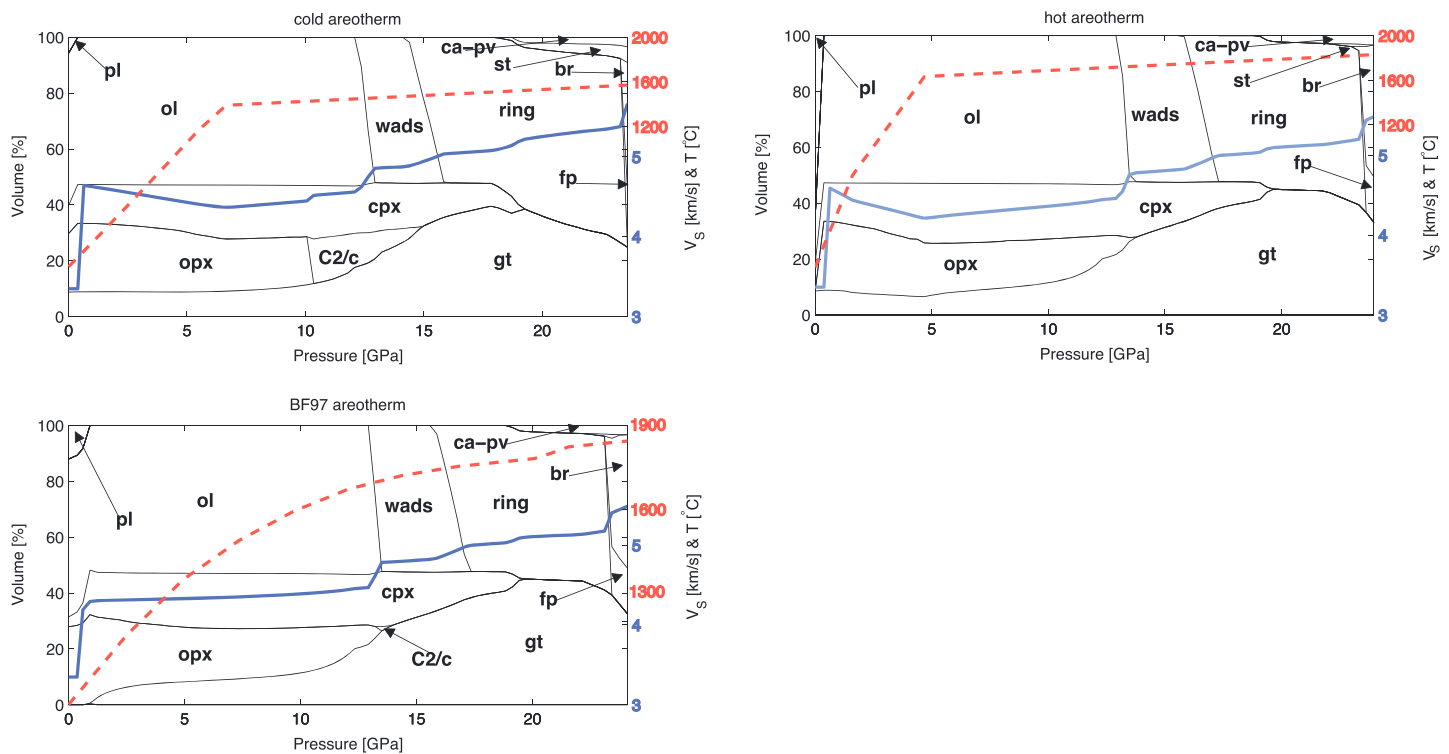


Figure 1. Examples of Martian mantle phase equilibria and corresponding shear wave speed profiles (solid blue lines) for the DW model Martian mantle composition (Table 1) along three different thermal profiles (dashed red lines): “cold” (left) and “hot” (right) areotherms (dashed lines) are from Verhoeven et al. (2005), whereas “BF97 areotherm” refers to the thermal conditions of the experimental study of Bertka and Fei (1997). Core radius is fixed to 1,389 km. Phases are olivine (ol), clinopyroxene (cpx), orthopyroxene (opx), spinel (sp), high-pressure polymorph of cpx (C2/c), garnet (gt), wadsleyite (wad), ringwoodite (ring), akimotoite (aki), calcium perovskite (ca-pv), ferriperovskite (fp), and bridgmanite (br).

the major lower mantle minerals ferriperovskite and bridgmanite stabilize. However, the stability of these silicates depends strongly on temperature and pressure conditions at the core-mantle boundary (CMB). Large cores will result in a lower mantle that is either thin or absent altogether, whereas higher temperatures will tend to stabilize bridgmanite at lower pressures (see Figure 1 and discussion below). The existence of a bridgmanite-dominated lower mantle is thus sensitive to the physical conditions at the CMB and Fe content of the core. Small cores tend to be Fe-rich and will favor presence of a lower mantle, whereas large cores will tend to be enriched in S and inhibit a lower mantle. Beyond this, presence of a lower mantle has implications for the dynamical evolution of Mars. Several studies have shown that a lower mantle is likely to exert considerable control over the dynamical evolution of mantle and core (e.g., Breuer et al., 1997; Harder & Christensen, 1996; van Thienen et al., 2006). In contrast, midmantle phase transitions are dynamically much less important and appear unlikely to prevent the entire mantle from convecting as a single unit (Ruedas et al., 2013a).

A related question is the current thermal state of Mars’s interior. While difficult to estimate directly, the areotherm represents, on a par with mantle and core composition, the most important parameter to be determined because of the fundamental control it exerts on physical structure. This is exemplified in Figure 1, which shows that phase equilibria, physical properties (here illustrated using shear wave speed), and presence of bridgmanite structure silicates in the lower mantle are very sensitive to the exact thermal conditions inside the Martian mantle. Current geophysical studies typically approach this problem by assuming examples of cold and hot mantle conditions (e.g., Khan & Connolly, 2008; Longhi et al., 1992; Rivoldini et al., 2011; Sohl & Spohn, 1997; Sohl et al., 2005; Van Hoolst et al., 2003; Verhoeven et al., 2005; Zharkov & Gudkova, 2005). Likewise, the areotherm considered in the experimental approach of Bertka and Fei (1997) is representative of hot conditions based on the need for achieving thermodynamic equilibrium experimentally. Thus, while the bulk chemical composition of Mars holds the potential of constraining many aspects of Mars such as internal structure, origin, and evolution, current constraints are not strong enough to reliably determine these unequivocally.

As observed experimentally (e.g., Jackson et al., 2002; McCarthy et al., 2011; Takei et al., 2014), viscoelastically based dissipation models impose strong constraints on the thermal state of the interior of a planet. This was tested by Nimmo and Faul (2013), whose model calculations showed that Martian global tidal dissipation, based on an extended Burgers formulation of viscoelasticity (to be described in section 3.4), is not only strongly temperature controlled but also frequency dependent. Similar conclusions were reached by Bellis and Holtzman (2014) in an analysis of the sensitivity of seismic wave propagation in a frequency-dependent anelastic model of Earth's upper mantle. Here we build upon the study of Nimmo and Faul (2013) and embed the viscoelastic model into our joint geophysical-thermodynamic framework. This extends previous studies of, for example, Khan and Connolly (2008) and Rivoldini et al. (2011) to proper consideration of the influence of dissipation on interior structure. In particular, earlier studies had difficulty in constraining the thermal structure of the mantle.

3. Geophysical Analysis

3.1. Background

In the present analysis, we focus on the tide raised on Mars by its moon Phobos and the Sun, which results in an imposed potential ψ that will cause Mars to deform and give rise to an induced potential ψ' according to

$$\psi'_n(\mathbf{r}) = \left(\frac{R}{r}\right)^{n+1} k_n \psi_n(\mathbf{R}, \mathbf{r}^*), \quad (1)$$

where R is the radius of the planet, \mathbf{R} is a point on the planet's surface, \mathbf{r} is an exterior point above the point \mathbf{R} , while \mathbf{r}^* is the position of the perturbing body. The potentials are expanded in terms of spherical harmonics of degree n and the proportionality constants, k_n , are tidal Love numbers of degree n and determine the amplitude of the response (e.g., Efroimsky, 2012a).

The above expression (1) for the amended potential of the tidally deformed planet stays valid insofar as the planet's response is purely elastic. In this approximation, the tidal bulge raised on Mars by Phobos is aligned with the direction from the planet's center toward Phobos, with no lagging. This ensures that both the torque applied by Phobos on Mars and the opposite torque with which Mars is acting on Phobos are 0.

Hence, in the elastic approximation, the tides on Mars make no influence on Phobos' semimajor axis, eccentricity, or inclination, and, as a consequence, no tidal heat is generated in Mars.

Realistic objects deviate from elasticity. So the tidal bulge acquires a complex structure and is no longer aimed at the perturbing body. Decomposition of the bulge over the tidal Fourier modes renders harmonics, some of which lag and some advance relative to the subsatellite point. Whatever the sign of the lag, each harmonic now produces tidal heat. In this situation (following Efroimsky & Makarov, 2014), expression (1) above should be written, in the time domain, as

$$\psi'_n(\mathbf{r}, t) = \left(\frac{R}{r}\right)^{n+1} \hat{k}_n \psi_n(\mathbf{R}, \mathbf{r}^*), \quad (2)$$

where \hat{k}_n is a linear operator (Love operator) mapping the entire history of the perturbation ($\psi_n(t')$ over $t' \leq t$) on the value of ψ' at the present time t . In the time domain, this is a convolution:

$$\psi'_n(\mathbf{r}, t) = \int_{t'=-\infty}^t \left(\frac{R}{r}\right)^{n+1} \dot{k}_n(t-t') \psi_n(\mathbf{R}, \mathbf{r}^*, t') dt', \quad (3)$$

while in the frequency domain it is a product of Fourier components:

$$\bar{\psi}'_n(\mathbf{r}, \omega_{pq}^{nm}) = \left(\frac{R}{r}\right)^{n+1} \bar{k}_n(\omega_{pq}^{nm}) \bar{\psi}_n(\mathbf{R}, \mathbf{r}^*, \omega_{pq}^{nm}), \quad (4)$$

ω_{pq}^{nm} being the Fourier tidal modes (whose absolute values are the physical forcing frequencies exerted in the material) and $\{pq\}^{nm}$ integers used to number the modes. In the former expression, \dot{k}_n denotes a time derivative, while in the latter expression, we employ overbars to emphasize that the Fourier components are complex, that is,

$$\bar{k}_n(\omega') = \text{Re} [\bar{k}_n(\omega')] + i \text{Im} [\bar{k}_n(\omega')] = |\bar{k}_n| e^{-\epsilon_n(\omega')}, \quad (5)$$

where we employed $\omega' = \omega_{pq}^{nm}$ for shorthand notation. In expression (4), $\bar{\psi}'_n(\mathbf{r}, \omega_{pq}^{nm})$ is lagging behind $\bar{\psi}_n(\mathbf{R}, \mathbf{r}^*, \omega_{pq}^{nm})$ by the phase angle $\epsilon_n(\omega_{pq}^{nm})$, which by convention is the negative argument of the complex

Love number $\bar{k}_n(\omega_{pq}^{nm})$. By setting \mathbf{r} equal to the position \mathbf{r}^* of the perturbing body, we obtain the additional potential “felt” by the latter (Phobos).

From the above expression, it is also possible to calculate the tidal torque, the radial elevation, and the tidal power dissipated in the planet. It turns out that at each tidal mode ω_{pq}^{nm} , an appropriate Fourier contribution into each of these quantities is proportional to the sine of the phase lag at that mode (e.g., Efroimsky, 2012a; Efroimsky & Makarov, 2014). The quantity inverse to the absolute value of this sine is conventionally named the tidal quality factor and denoted with Q_n and defined as

$$\frac{1}{Q_n(\omega_{pq}^{nm})} = \sin |\epsilon_n(\omega_{pq}^{nm})|. \quad (6)$$

The functional form of the frequency dependence of the tidal quality factors is different for different degrees n (see, e.g., Efroimsky, 2015). Fortunately, this difference becomes manifest only at extremely low frequencies. At ordinary frequencies, these quality factors are very close to the nominal (“seismic”) quality factor Q , which is usually defined through the relation

$$\frac{1}{Q} = \frac{1}{2\pi\mathcal{E}'} \oint \frac{\partial \mathcal{E}}{\partial t} dt, \quad (7)$$

where \mathcal{E} and \mathcal{E}' refer to the energy and peak energy over one cycle and the integral is taken over the same. The expression on the right-hand side of equation (7) turns out to be equal to the absolute value of the sine of the phase lag between strain and stress (see, e.g., equations (45)–(47) in Efroimsky, 2015). For ordinary (not too low) frequencies, the tidal phase lag ϵ virtually coincides with the phase lag between the strain and the stress in the material. Accordingly, at not too low frequencies the tidal Q_n virtually coincides with the nominal seismic Q .

In the following, we shall concentrate on the semidiurnal tidal mode for which $\{\frac{nm}{pq}\} = \{\frac{22}{00}\}$; so we shall be dealing with k_2 and Q_2 (henceforth labeled k_2 and Q).

While both k_2 and Q depend on interior properties such as density and rigidity, Q is strongly sensitive to viscosity and, thus, temperature and grain size. This will be described in more detail in section 3.4.

3.2. Geophysical Data

There are currently few geophysical data available that bear directly on the deep interior structure of Mars. Here we shall focus on mean density ($\hat{\rho}$), mean moment of inertia (I/MR^2), second-degree tidal Love number (k_2), and global tidal dissipation or tidal quality factor (Q). Mean density and moment of inertia are sensitive to the density structure of the planet, whereas the sensitivity of the second-degree tidal Love number and global tidal dissipation is more complex.

The geophysical data for Mars employed here are summarized in Table 2 and are discussed in more detail in the literature (e.g., Balmino et al., 2005; Bills et al., 2005; Genova et al., 2016; Jacobson, 2010; Konopliv et al., 2006, 2011, 2016; Lainey et al., 2007; Marty et al., 2009; Nimmo & Faul, 2013; Rivoldini et al., 2011; Van Hoolst et al., 2003; Yoder et al., 2003; Zharkov & Gudkova, 2005, 2009, 1997). The k_2 estimates determined from orbiting spacecraft data (e.g., Genova et al., 2016; Konopliv et al., 2006, 2011; Yoder et al., 2003) are consistent with values ranging from ~ 0.13 to 0.175 (except the Marty et al., 2009, determination) and typically refer to the period of the solar (semidiurnal) tide (12 h 19 min). Current Q estimates range from ~ 70 to 110 and indicate that Mars is more dissipative than the solid Earth (270 ± 80) at the equivalent diurnal period (Ray et al., 2001).

Here we employ the most recent spacecraft-determined value of $k_2 = 0.169 \pm 0.006$ by Konopliv et al. (2016). Independent analysis by Genova et al. (2016) of spacecraft tracking data also resulted in $k_2 = 0.1697 \pm 0.0009$. These values are considered at the solar period. To change to k_2 at the main tidal period of Phobos (5.55 h), consideration of the effect of anelasticity on k_2 and Q to account for the proper frequency dependence is included through the viscoelastic formulation (section 3.4). The resultant changes are found to be $\ll 1\%$. Similar results were also obtained by Zharkov and Gudkova (2005).

To determine the tidal dissipation factor at the period of Phobos, we follow Zharkov and Gudkova (2005) and relate the mean dissipative factor Q to the tidal lag angle (ϵ) using expressions (6) and (7) above

$$\sin \epsilon \approx \epsilon = \frac{1}{Q}. \quad (8)$$

Table 2
 Summary of Martian Geophysical Data, Uncertainties, and Sources

Observation	Symbol	Value (\pm uncertainty)	Source
Mean density	$\bar{\rho}$	$3.9350 \pm 0.0012 \text{ g/cm}^3$	Rivoldini et al. (2011)
Mean moment of inertia	I/MR^2	0.36379 ± 0.0001	Konopliv et al. (2016)
Love number	k_2	0.169 ± 0.006	Konopliv et al. (2016)
Dissipation	Q	95 ± 10	This study
Mean radius	R	3,389.5 km	Seidelmann et al. (2002)
Mean mass	M	$6.417 \cdot 10^{23} \pm 2.981 \cdot 10^{19} \text{ kg}$	Konopliv et al. (2016)

Note. k_2 and Q are evaluated at the main tidal period of Phobos (5.55 h). The values for the mean moment of inertia and mass have been updated by Rivoldini using the latest determination of GM for Mars with $G = 6.67408(31) 10^{11} \text{ m}^3 \text{ kg s}^{-2}$ (Konopliv et al., 2016).

Relying on parameters relevant to the Mars-Phobos system, as summarized in Yoder, (1995), Zharkov and Gudkova (2005) find

$$\frac{Q}{k_2} = \frac{1}{\epsilon k_2} = 559. \quad (9)$$

From this expression, we obtain $Q \sim 91 - 100$ at the tidal period of Phobos. This value agrees reasonably well with the estimates made by Bills et al. (2005), Lainey et al. (2007), Jacobson (2010), Nimmo and Faul (2013), and Yoder et al. (2003), who determined Q_s of 92 ± 11 , ~ 85 , ~ 80 , ~ 83 , and 88 ± 16 , respectively. In obtaining these estimates, Bills et al. (2005) used a value for k_2 (0.0745) that is too low given current understanding, while Lainey et al. (2007) and Jacobson (2010) relied on the same k_2 value by Konopliv et al. (2006). For comparison, Nimmo and Faul (2013), who used the Yoder et al. (2003) solar tide k_2 value (0.149 ± 0.017), found a 0.6% change in k_2 when converting to the synodic period of Phobos (erroneously referred to as 11.1 h) and obtained 0.148 ± 0.017 . To determine Q , Nimmo and Faul (2013) employ the estimate of Lainey et al. (2007) but correct for the influence of higher-degree terms (k_3 and k_4) on the orbit of Phobos (see discussion below). Assuming certain ranges for the ratios k_2/k_3 and k_3/k_4 , the authors obtain a Q estimate of 88 ± 16 . Earlier analyses of the orbital acceleration of Phobos estimated the tidal Q of Mars to be 100 ± 50 (Lambeck, 1979; Smith & Born, 1976; Yoder, 1982).

Because of the proximity of Phobos to Mars (mean distance 9,378 km), higher-degree terms (e.g., k_3 , k_4 , ...) appear to be significant for the orbital evolution of Phobos (Bills et al., 2005; Konopliv et al., 2011). Based on model values of k_3 and k_4 , Zharkov and Gudkova (2005) and Konopliv et al. (2011) considered the correction that would be introduced by including higher-order terms and found that this contributes less than 10% to the tidal deceleration of Phobos. In contrast, Lainey et al. (2007) considered only the degree-2 term, given that degree-3 and degree-4 terms are not known, and argued that the tidal dissipation factor Q should be considered as an effective Q that partly absorbs losses from higher harmonics. A reasonable alternative would be to compensate by increasing the error bars (V. Lainey, personal communication, 2017), as a result of which of we set $Q = 95 \pm 10$. Additionally, tidal forcing at degree-2 will induce tidal waves at periods other than the main tide considered here (Roosbeek, 1999). However, the amplitudes of the tidal waves at the other periods are much smaller. The next largest amplitude in the subdiurnal spectrum, for example, is a factor of ~ 7 smaller than the amplitude of the main Phobos-induced tide at 5.55 h (Van Hoolst et al., 2003). Hence, we neglect their contribution here.

3.3. Crust and Mantle Model

Following our previous work (e.g., Khan & Connolly, 2008), Gibbs free-energy minimization is employed (Connolly, 2009) to compute stable mantle mineralogy and physical properties along self-consistent mantle adiabats for each of the five model mantle compositions listed in Table 1 using the NCFMAS model chemical system comprising the oxides CaO-FeO-MgO-Al₂O₃-SiO₂-Na₂O. We rely on the thermodynamic formulation of Stixrude and Lithgow-Bertelloni (2005b) and parameters of Stixrude and Lithgow-Bertelloni (2011). In the crust and lithosphere, temperature is computed by a linear thermal gradient, which for each model is determined from surface temperature and temperature and thickness of the lithosphere. This assumption implies that no crustal radioactivity is present. Although this is unlikely to be realistic, crustal structure has little

influence because the data considered here are not really sensitive to it. As a consequence, the exact nature of the crustal geotherm is not important. The assumption of thermodynamic equilibrium is debatable at low temperature (e.g., Wood & Holloway, 1984). As a result, if for a given model a mineralogy at a temperature below 800°C is required, equilibrium mineralogy was computed at 800°C, whereas physical properties for the mineralogy are determined at the actual temperature of interest. The crust is likely to be more complex lithologically, not equilibrated, and is probably porous. The effect of porosity is taken into account through a decrease in the seismic properties of the crust. The latter will be described further in section 4.1. The fixed crustal composition employed here is also summarized in Table 1.

Deficiency of experimental constraints on the parameters relevant for the thermodynamic formalism and parameterization of Stixrude and Lithgow-Bertelloni (2011) are the major source of uncertainty in the thermodynamic calculations. Elastic moduli and density have been estimated to be accurate to within ~0.5 and ~1–2%, respectively (Connolly & Khan, 2016).

3.4. Viscoelastic Model

The dissipation model adopted here is described in detail in Jackson and Faul (2010) and relies on laboratory experiments of torsional forced oscillation data on melt-free polycrystalline olivine. Broadly similar results have also been obtained by other groups (e.g., Takei et al., 2014). In what follows we base ourselves on Jackson and Faul (2010) and only provide a summary description here.

In the Earth, Moon, and Mars, and in the absence of melting, dissipation (Q) has been observed to be frequency dependent $1/Q \sim \omega^{-\alpha}$, where ω is angular frequency and α is a constant (e.g., Efroimsky & Lainey, 2007) that has been observed to lie in the range 0.1–0.4 (e.g., Benjamin et al., 2006; Jackson et al., 2002; Minster & Anderson, 1981). Since Maxwellian viscoelasticity is unable to reproduce this frequency dependence, other rheological models (for a review see, e.g., Karato, 2008) such as the extended Burgers model of Jackson and Faul (2010) have been proposed. Jackson and Faul (2010) argue for the extended Burgers model over other rheological models because it describes the changeover from (anharmonic) elasticity to grain size-sensitive viscoelastic behavior, whereby it is able to explain the observed dissipation in the laboratory experiments on olivine (Jackson & Faul, 2010).

The response of a viscoelastic material can be described in terms of the complex frequency-dependent compliance $\hat{J}(\omega) = J_R(\omega) + iJ_I(\omega)$, where $i = \sqrt{-1}$, and subscripts R and I denote real and complex parts, respectively. For the extended Burgers model of Jackson and Faul (2010), $J_R(\omega)$ and $J_I(\omega)$ can be written as

$$J_R(\omega) = \frac{1}{\mu_U} \left[1 + \Delta \int_{\tau_L}^{\tau_H} \frac{D(\tau)}{1 + \omega^2 \tau^2} d\tau \right] \quad (10)$$

$$J_I(\omega) = \frac{1}{\mu_U} \left[\omega \Delta \int_{\tau_L}^{\tau_H} \frac{\tau D(\tau)}{1 + \omega^2 \tau^2} d\tau + \frac{1}{\omega \tau_M} \right], \quad (11)$$

which is essentially the Laplace transform of the creep function for the extended Burgers model of linear viscoelasticity (see, e.g., Jackson & Faul, 2010).

In these expressions, μ_U represents the unrelaxed, that is, infinite-frequency, shear modulus, τ period, $\tau_M = \eta/\mu_U$ Maxwell viscous relaxation time, η viscosity, Δ strength of relaxation mechanism, and $D(\tau)$ distribution of relaxation times. From the above equations, local dissipation ($1/Q$) and shear modulus (μ) at a particular frequency can be computed from $1/Q = |J_I|/\sqrt{J_I^2 + J_R^2} \approx |J_I|/|J_R|$ and $\mu(\omega) = 1/\sqrt{J_R^2(\omega) + J_I^2(\omega)}$, respectively.

The advantage with this model is that $D(\tau)$ can be used to specify a distribution of anelastic relaxation times accounting for the monotonic background dissipation (D_B) and the superimposed dissipation peak (D_p) of elastically accommodated grain boundary sliding (Jackson et al., 2014), in addition to the associated modulus dispersion (Jackson & Faul, 2010). D_B is given by

$$D_B(\tau) = \frac{\alpha \tau^{\alpha-1}}{\tau_H^\alpha - \tau_L^\alpha}, \quad (12)$$

where τ_L and τ_H are the integration limits corresponding to short and long periods, respectively. $0 < \alpha < 1$ for $\tau_L < \tau < \tau_H$ and 0 elsewhere with associated relaxation strength Δ_B (Minster & Anderson, 1981). In the

low-frequency limit, J_l (equation (11)) reduces to Maxwellian behavior ($J_l = 1/\omega\eta$). To model the dissipation peak D_p that appears superimposed on the background, a term of the following form needs to be added

$$D_p(\tau) = \frac{1}{\tau\sigma\sqrt{2\pi}} \exp\left[-\frac{\ln^2(\tau/\tau_p)}{2\sigma^2}\right], \quad (13)$$

where τ_p indicates position of the peak with peak width σ and associated relaxation strength Δ_p . This peak is found to occur at low temperature and/or short time scales and corresponds to elastically accommodated grain boundary sliding.

The timescales τ_L , τ_H , τ_M , and τ_p are all temperature (T), pressure (P), and grain-size (d_{grain}) dependent, which for each individual timescale is modeled using

$$\tau(P, T, d_{\text{grain}}) = \tau_0 \left[\frac{d_{\text{grain}}}{d_0}\right]^m \exp\left[\frac{E}{R}\left(\frac{1}{T} - \frac{1}{T_0}\right)\right] \exp\left[\frac{V}{R}\left(\frac{P}{T} - \frac{P_0}{T_0}\right)\right], \quad (14)$$

where τ_0 is a normalized value at a particular set of reference conditions P_0 (0.2 GPa), T_0 (900°C), and d_0 (13.4 μm), and E and V are activation energy and volume, respectively. In addition, different grain-size exponents m for anelastic and long-term viscous creep processes are allowed for. All of the above constants are tabulated in Nimmo et al. (2012) and Nimmo and Faul (2013), except for d_{grain} , α , E , and V , which are considered variable parameters (see section 4.1).

This model can now be directly linked with the thermodynamic computations in that the latter provides the unrelaxed (infinite-frequency) shear modulus μ_U that appears in the above equations, in addition to P and T and any other thermodynamic variables needed (all functions of radius). Note that the shear moduli are computed on the basis of thermochemical models of Mars and are constrained by geophysical data, hence the improvement here over previous studies that had little control over internal structure parameters required as input (e.g., Bills et al., 2005; Nimmo & Faul, 2013; Nimmo et al., 2012; Sohl & Spohn, 1997; Sohl et al., 2005). Finally, to compute global frequency-dependent k_2 and Q from the model outlined above, we employ the viscoelastic tidal code of Roberts and Nimmo (2008). This code assumes spherical symmetry and that all dissipation occurs in shear; for numerical reasons, we imposed a viscosity cutoff of 10^{29} Pa s.

3.5. Core Model

Mass-radius relations of rocky planets generally require Fe-rich metallic cores alloyed with a light element such as Si, C, or S (e.g., Birch, 1964; Poirier, 2000). In the case of Mars, it is argued that S is the dominant light element because the other candidates do not have sufficient solubility in iron-rich liquid at the relatively low pressures that would have been maintained during core formation (e.g., Stevenson, 2001). Evidence in support of this is the observed depletion of chalcophile elements, notably S, of the SNCs (see section 2.1). Accordingly, an Fe-S core is generally assumed in geophysical models of Mars. To date, the most elaborate parameterization of the Martian core (in the Fe-FeS system) is that of Rivoldini et al. (2011). Here we follow Rivoldini et al. (2011) and assume that Mars's core is well mixed and convecting. To compute depth-dependent thermoelastic properties for the core, we use equations of state for liquid iron and liquid iron-sulfur alloys.

Core pressure is obtained from the hydrostatic equation

$$\frac{dP(r)}{dr} = -\rho(r)g(r), \quad (15)$$

where r is radius, ρ density, and g gravitational acceleration. g also obeys the Poisson equation

$$\frac{dg(r)}{dr} + \frac{2g(r)}{r} = 4\pi G\rho(r), \quad (16)$$

where G is the gravitational constant. For a well-mixed and vigorously convecting core the temperature gradient is given by

$$\frac{dT(r)}{dr} = -T(r)\frac{\gamma(r)}{K_S(r)}\rho(r)g(r), \quad (17)$$

where γ is the Grüneisen parameter and K_S is adiabatic bulk modulus. These ordinary differential equations are solved numerically (Brankin et al., 1993) subject to the following boundary conditions

$$P(r_{\text{cmb}}) = P_{\text{cmb}} \quad (18)$$

$$T(r_{\text{cmb}}) = T_{\text{cmb}} \quad (19)$$

$$g(0) = 0 \quad (20)$$

where r_{cmb} , P_{cmb} , and T_{cmb} are radius, pressure, and temperature at the CMB, respectively. These quantities on the mantle side of the CMB are those determined in section 3.3.

The thermoelastic quantities ρ , K_S , and γ depend on pressure, temperature, and core composition (S content) and are calculated using the approach outlined in Appendix A.

4. Computational Aspects

4.1. Model Parameterization

In the following we briefly describe model parameterization, which is illustrated in Figure 2. For present purposes, we assume our model of Mars to be spherically symmetric and have divided it into three layers comprising crust, mantle, and core. The crust has been further subdivided into an additional three layers that are parameterized in terms of P and S wave velocity, density, and Moho thickness. Rather than varying V_p , V_s , and ρ independently in the crust, however, we introduced a variable parameter (ϕ) to mimic the effect of porosity and computed the aforementioned physical properties using $x'_i = x_i \cdot \phi_i$, where x_i are thermodynamically computed V_p , V_s , and ρ (section 3.3) in crustal layer i . ϕ_i is determined from $\phi_i = \phi_0 + (1 - \phi_0) \cdot i/N$ with ϕ_0 being variable surface porosity and N the total number of crustal layers. This parameterization ensures that crustal properties increase from the surface down to the Moho where porosity is expected to vanish due to pressure (i.e., $1 - \phi_i = 0$). Because of the imposed viscosity cutoff (see section 3.4), we fixed shear attenuation in the conductive regions (crust and upper lithosphere) to 600 based on terrestrial experience. The sublithospheric mantle is assumed to be uniform and modeled using the variables composition (in the NCFMAS system) and mantle temperature. Within the lithosphere, temperature is computed by a linear areothermal gradient, which for each model iteration is determined from the variables T_{surf} , T_{lit} , and d_{lit} . The sublithospheric mantle adiabat is defined by the entropy of the lithology at the temperature T_{lit} , that is, at the base of the lithosphere of thickness d_{lit} . The bottom of the lithosphere is defined as the location where the conductive lithospheric geotherm intersects the mantle adiabat. Since the viscoelastic model (section 3.4) is grain size dependent, the model is additionally parameterized in terms of a single grain size (d_{grain}). Many of the parameters belonging to the viscoelastic model are determined experimentally and therefore uncertain. To better capture this, we included α , E , and V as variable parameters. Uncertainty ranges are taken from Jackson and Faul (2010). The mantle pressure profile is obtained by integrating the vertical load from the surface pressure boundary condition. Core parameters include radius, composition (S content), and the input parameters required to compute physical properties of the core are those determined by integrating the load from the surface to the CMB and the entropy of the lithology at T_{lit} , which determines the temperature at the CMB (section 3.5). Given values of all of the above model parameters, the forward model can be solved.

4.2. Forward Problem

The forward model consists of computing geodetic data ($\bar{\rho}$, l/MR^2 , k_2 , Q) from a knowledge of the physical structure of the crust and thermochemical structure of mantle and core. To determine stable mineralogy (\mathcal{M}), isotropic shear (μ) and bulk (κ) moduli, density (ρ), and attenuation structure (here designated by complex moduli $\hat{\mu}$ and $\hat{\kappa}$) along self-consistent mantle adiabats, we employ Gibbs free-energy minimization and a grain size-dependent viscoelastic formulation. With this, the forward problem can be written as

$$\underbrace{\{X_m, T_{\text{lit}}, d_{\text{lit}}, d_{\text{grain}}, \dots, r_{\text{core}}, X_S\}}_{\text{primary parameters}} \xrightarrow[\text{operator}]{g_1} \mathcal{M} \xrightarrow{g_2, g_3} \{\rho, \hat{\mu}, \hat{\kappa}\} \xrightarrow{g_4} \underbrace{\{\bar{\rho}, l/MR^2, k_2, Q\}}_{\text{data}}$$

where the primary parameters are those described above in section 4.1 and the other parameters (\mathcal{M} , $\hat{\mu}$, $\hat{\kappa}$, ...) represent secondary parameters that are required for the purpose of computing data (section 3.2). The operators (g_1, \dots, g_4) represent the various forward models, for example, Gibbs free energy minimization (section 3.3), extended Burgers model and viscoelastic tidal response (section 3.4).

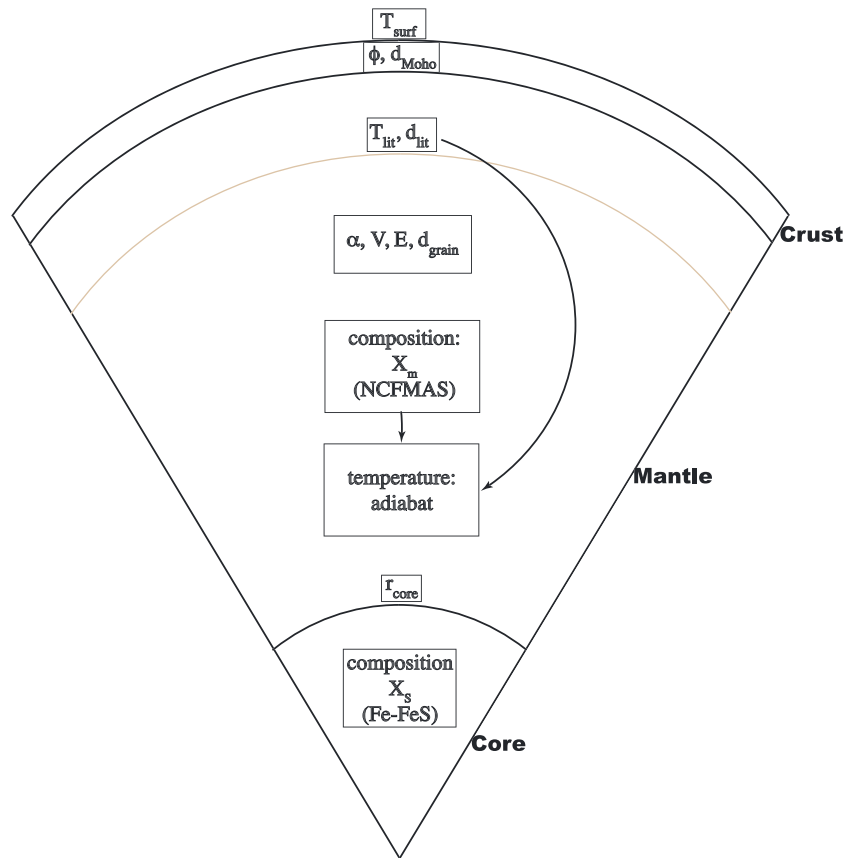


Figure 2. Schematic diagram illustrating model parameterization. The model is spherically symmetric and is parameterized using the following parameters. Crust: porosity (ϕ) and crustal thickness (d_{Moho}); mantle: lithospheric thickness (d_{lit}), entropy of lithology at the temperature at the bottom of the lithosphere (T_{lit}), composition (X_m), grain size (d_{grain}), activation volume (V) and energy (E), and frequency exponent (α). Core: composition (X_s) and radius (r_{core}). For more details see main text (section 4.1). The arrow indicates that the mantle adiabat is determined from X_m , d_{lit} , and T_{lit} .

4.3. Inverse Problem

To solve the inverse problem $\mathbf{d} = g(\mathbf{m})$, where \mathbf{d} is a data vector consisting of observations and g is an operator that maps from the model space into the data space, we employ a Bayesian approach as outlined in Mosegaard and Tarantola (1995)

$$\sigma(\mathbf{m}) = k \cdot h(\mathbf{m})\mathcal{L}(\mathbf{m}), \tag{21}$$

where $h(\mathbf{m})$ is the prior model parameter probability distribution, that is, the information on model parameters procured independently of data, $\mathcal{L}(\mathbf{m})$ is the likelihood function, which measures the misfit between observed and predicted data, k is a normalization constant, and $\sigma(\mathbf{m})$ is the posterior model parameter distribution. $\sigma(\mathbf{m})$ represents the solution to the inverse problem above. $\mathcal{L}(\mathbf{m})$ is determined from the observed data, data uncertainties, and the manner in which the latter are used in modeling data noise (to be described in the following).

The Metropolis algorithm is employed to sample the posterior distribution (equation (21)) in the model space (Mosegaard & Tarantola, 1995). This algorithm, which samples the model space in a random fashion, is an importance sampling algorithm, that is, it ensures that models that fit data well and are simultaneously consistent with prior information are sampled more frequently. The Metropolis algorithm samples the model space with a sampling density that is proportional to the (target) posterior probability density and thus ensures that low-probability areas are sampled less excessively. This is an important feature of any algorithm that wishes to randomly sample high-dimensional model spaces where the probability density over large proportions of the volume are near 0.

Table 3
Prior Information on Primary Model Parameters

Description	Quantity	Parameter	Value/range	Distribution
Surface porosity	1	ϕ_0	0.5–0.65	Uniform
Surface temperature	1	T_{surf}	0–727°C	Log-uniform
Crustal thickness	1	d_{Moho}	10–80 km	Log-uniform
Crustal composition (in the NCFMAS system)	5	X_c	See Table 1	Fixed
Shear attenuation in crust and lithosphere	1	Q_μ	600	Fixed
Entropy of lithology at the temperature at the bottom of the lithosphere	1	T_{lit}	727–1427°C	Log-uniform
Lithospheric depth (depth to intersection of conductive lithospheric geotherm and mantle adiabat)	1	d_{lit}	100–600 km	Log-uniform
Mantle composition (in the NCFMAS system)	5	X_m	±10% around the Values given in Table 1	Log-uniform
Grain size	1	d_{grain}	0–50 mm	Uniform
Frequency exponent	1	α	0.2–0.4	Log-uniform
Activation energy	1	E	300–400 kJ/mol	Log-uniform
Activation volume	1	V	10^{-6} – 10^{-5} m ³ /mol	Log-uniform
Core radius	1	r_{core}	0–3,000 km	Log-uniform
Core composition (Sulfur content)	1	X_S	0–100 wt%	Log-uniform

Note. Model parameterization is illustrated in Figure 2.

4.4. Prior Information

The prior model parameter information described above is summarized in Table 3 below. The chosen prior ranges represent the information acquired from data and results from experimental studies supplemented with results from numerical studies as discussed in the foregoing sections. The prior range on surface temperature is relatively large but reflects the fact that the data considered here have little sensitivity on crustal and subcrustal lithospheric thermal structure. This has little effect on computed physical properties of the crustal and subcrustal structure as tests have shown where surface temperature was fixed to that of present-day Mars. Hence, in what follows the thermal structure of the crust and subcrustal lithosphere will not be discussed further.

4.5. Sampling the Posterior

Under the assumption that data noise is Gaussian distributed and that observational uncertainties and calculation errors among the data sets considered are independent, the likelihood function can be written as

$$\mathcal{L}(\mathbf{m}) \propto \prod_i \exp\left(-\frac{|d_{\text{obs}}^i - d_{\text{cal}}^i(\mathbf{m})|^2}{2\sigma_i^2}\right) \quad (22)$$

where i runs over $\bar{\rho}$, I/MR^2 , k_2 , and Q , d_{obs} and $d_{\text{cal}}(\mathbf{m})$ denote observed and calculated data, respectively, and σ data uncertainty.

5. Results and Discussion

5.1. Data Fit

Data fits for all five major compositions (Table 1) are summarized in Figure 3. The various compositions are all capable of fitting mean density and moment of inertia, in addition to global tidal dissipation, but show scatter

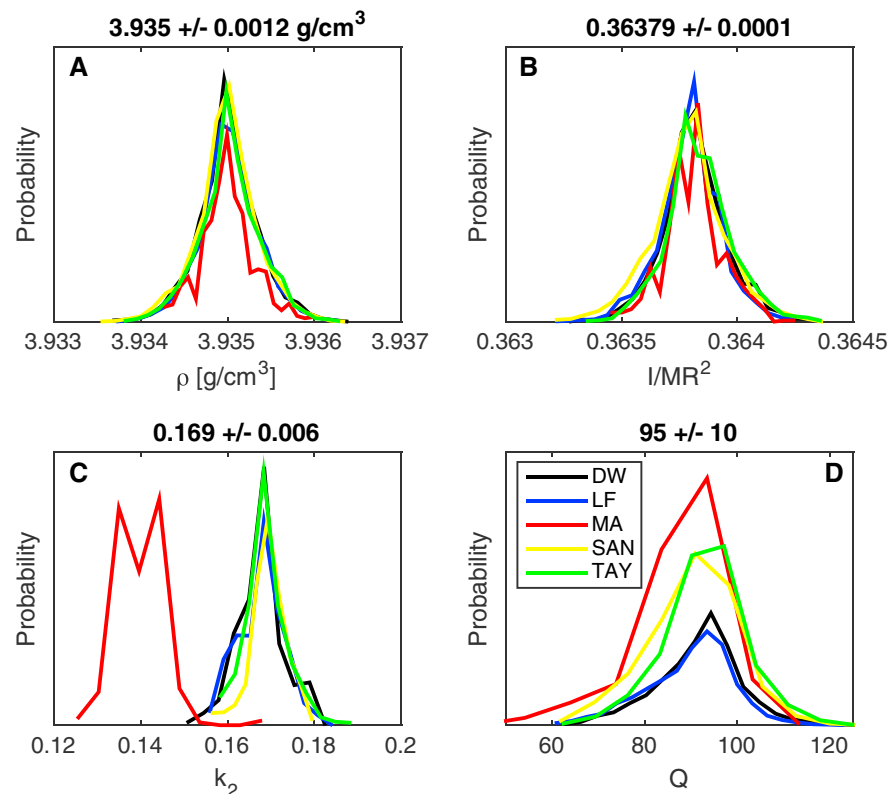


Figure 3. Probability distributions showing fit to individual data (observed value indicated on top of each plot) for each of the inverted compositions (defined in Table 1): mean density (a); mean moment of inertia (b); second-degree tidal Love number (c); and global tidal dissipation (d). The results shown in (c) and (d) refer to the main tidal period of Phobos (5.55 h).

in k_2 , particularly compositional model MA. The discrepancy between MA and the other compositions arises because MA produces more rigid models (~3–5% higher S wave velocity) in the depth range 100–1,100 km relative to the other models. This is principally due to presence of garnet-rich phases. This, coupled with smaller core sizes, results in the inability of MA to fit k_2 . Given the geochemical point made earlier (section 2.1) that MA represents a somewhat exotic composition and is probably unlikely to be representative of the bulk composition of Mars, we discard MA from further analysis.

5.2. Mantle Temperature Profiles

Inverted present-day areothermal profiles are shown in Figure 4. For comparison, we are also showing sampled prior areotherms, which span a very large temperature range. Inverted models are comparatively well constrained over most of the mantle and core. In comparison to the prior ranges (Table 3), both d_{lit} and T_{lit} are relatively well constrained with overlapping estimates in the range 200–400 km and ~1400–1460°C. The mantle adiabats show “structure” at depths around 1,000–1,100 km and 1,300–1,400 km, respectively, that is, at the locations where the major mantle mineral phase transitions occur (olivine→wadsleyite and wadsleyite→ringwoodite). At the CMB, temperatures in the range 1600–1700°C are obtained. Differences between inverted areotherms for all four bulk compositions are relatively small and are unlikely to be large enough to enable us to distinguish between the bulk compositions based on the data considered here.

In Figure 4 we are also showing mean temperature profiles from a recent geodynamical study by Plesa et al. (2016). Plesa et al. (2016) modeled the thermal evolution of Mars to specifically investigate the spatial variation in present-day surface heat flux in anticipation of the InSight mission. The blue and pink lines show present-day hot and cold end-member average temperature profiles from Plesa et al. (2016) assuming a core size of 1,500 km. The comparison shows that the results from the inversion are bracketed by the end-member geodynamic models. For reference, we also included the recent present-day dry Martian solidus of Kiefer et al. (2015).

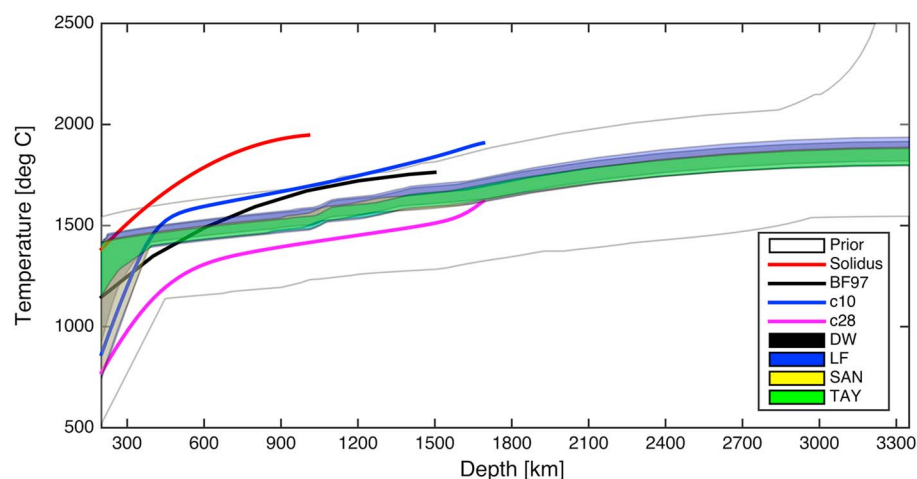


Figure 4. Sampled present-day mantle areotherms for the four main bulk compositions investigated here (defined in Table 1). The prior range and several areotherms from the literature are also shown: end-member profiles (c10 and c28) from the thermal evolution simulations by Plesa et al. (2016) and experimental data (BF97) after Bertka and Fei (1997). “Solidus” refers to the present-day dry Martian solidus of Kiefer et al. (2015). Note that relative to the legend, colors are less vivid because profiles have been plotted using a transparency factor. Thermal structure of crust and uppermost lithosphere is not shown.

Independent direct constraints on the thermal structure of Mars are few. Petrological estimates derive principally from Gamma Ray Spectrometer data (Mars Odyssey) for several major volcanic provinces (Baratoux et al., 2011) and analyses of shergottite meteorites (Filiberto & Dasgupta, 2015). These estimates bracket temperatures found here but are uncertain by several hundred degrees Celsius for dry mantle conditions and increase further if water and/or other volatiles are added (e.g., Balta & McSween, 2013; Filiberto et al., 2016).

No attempt was made to account for a thermal boundary layer between mantle and core. While a thin thermal boundary layer with a temperature difference of $\sim 100^\circ\text{C}$ is possible (e.g., Kiefer & Li, 2016), data are not sensitive enough to “see” such a layer. This was verified by investigating how an increase of 100°C across the CMB affects core properties. As expected, differences in, for example, P wave velocity and density on the core side of the CMB relative to a model without a thermal boundary layer amounted to $<0.5\%$, which from the point of view of the geophysical data is an insignificant change. Results are summarized in Table 4.

5.3. Grain Size

Sampled grain size distributions are shown in Figure 5 for the four main compositions. Except for TAY, the grain size distributions are fairly uniformly distributed in the millimeter-to-centimeter range (1–50 mm) but show a strong dropoff below 1 mm. This indicates that grain sizes are >1 mm in the Martian mantle but less well resolved in the range above. In addition, a grain size of ~ 2 –3 mm for model TAY appears to be preferred.

The importance of grain size arises because of the strong control it exerts on the diffusion creep rheology of the crust and mantle (viscosity $\propto d_{\text{grain}}^m$, $m = 2$ –3). As summarized by Karato, (2008, Ch. 13), common estimates of grain sizes of terrestrial rocks vary from 0.1 mm to 10 mm. Grain size estimates in the deeper Earth are invariably indirect with estimates ranging from small (μm) to relatively large grain sizes (cm), with a possible increase in grain size with depth (Karato & Wu, 1993). The latter would result from a change in deformation mechanism in Earth’s upper mantle where a transition from dislocation to diffusion creep occurs. The depth at which this transition occurs depends on a range of flow law parameters (Hirth & Kohlstedt, 2013).

In our inverse treatment, we neglect the complexity of a depth-dependent grain size. Based on the observation that the geodynamical simulations (section 6) suggest homogeneous grain sizes throughout Mars’ mantle, this appears to be a reasonable assumption. Generally, grain growth is temperature controlled and on Earth the lower mantle transition is expected to limit the size of grains as material is being moved across the transition and recrystallizes (e.g., Solomatov, 2001; Solomatov & Reese, 2008). In comparison, the mid-mantle phase transitions in the Martian mantle at ~ 13 GPa (1,100 km depth) and 15 GPa (1,300 km depth) (cf. Figure 1), respectively, are dynamically unimportant (Ruedas et al., 2013a). As a consequence, and in view

Table 4
Summary of Inversion Results

Parameter	DW	LF	SAN	TAY
Crust				
d_{moho} (km)	70–80	55–80	60–80	70–80
Lithosphere				
T_{lit} (°C)	1420–1440	1400–1460	1400–1440	1400–1420
d_{lit} (km)	220–320	200–350	275–400	200–300
Core				
T_{CMB} (°C)	1640–1680	1630–1690	1620–1660	1630–1670
T_{center} (°C)	2110–2160	2100–2180	2080–2140	2100–2150
P_{CMB} (GPa)	19–19.9	18.8–19.9	18.9–19.7	18.8–19.9
Fe (wt%)	81.5–84	82.2–85	82.5–84.5	81.5–83.5
S (wt%)	16–18.5	15–17.8	15.5–17.5	16.5–18.5
r_{core} (km)	1,720–1,810	1,725–1,810	1,730–1,800	1,730–1,810
Mass fractions				
Crust	0.04–0.048	0.03–0.05	0.035–0.05	0.04–0.048
Mantle	0.72–0.74	0.715–0.75	0.72–0.745	0.715–0.745
Core	0.215–0.24	0.22–0.24	0.22–0.235	0.22–0.24
Viscoelastic parameters				
d_{grain} (mm)	1–50	1–50	1–50	1–50
α	0.27–0.38	0.25–0.35	0.24–0.32	0.3–0.36
E (kJ/mol)	300–400	300–400	300–400	300–400
V ($\times 10^{-5}$ m ³ /mol)	1–10	1–10	1–10	1–10
BSM element ratios				
Mg/(Mg+Fe)	0.745	0.751	0.745	0.728
Mg/Si	1.01	0.97	1.04	0.85
Bulk Mars element ratios				
Fe/Ni	18	18	18	18
Fe/Si	0.89	0.87	0.84	0.91
Fe/Si (wt)	1.77	1.73	1.66	1.81

Note. Quoted ranges cover the 95% credible interval. Except for core-mantle boundary temperature (T_{CMB}), central core temperature (T_{center}), and core-mantle boundary pressure (P_{CMB}), all parameters are defined in Table 3. Bulk silicate mantle composition is abbreviated BSM. Bulk Mars elemental ratios assume a meteoritic Fe/Ni ratio and that a proportion of Fe contained in the core is replaced by Ni (see text for details). Elemental ratios are atomic unless otherwise noted (only mean compositions are quoted).

of an apparent absence of a lower mantle transition in Mars (see section 5.5), grain sizes in excess of 1 mm in the Martian mantle are not unrealistic.

For the baseline Martian model, Nimmo and Faul (2013) fixed $\alpha = 0.274$, whereas we generally find a slightly higher α in the range 0.3–0.4 (values for α , E , and V are summarized in Table 4). The reason for this difference is not clear but could possibly be related to Nimmo and Faul (2013) erroneously using 11.1 h instead of 5.55 h as forcing period.

Nimmo and Faul (2013) also observed a trade-off between grain size and mantle temperature (and lid thickness). This trade-off is not observed here. One reason for this is that in the inversion, models are “forced” to fit the measured k_2 and Q , whereas Nimmo and Faul (2013) are calculating k_2 and Q based on a range of input parameters and comparing these qualitatively to the observations. Thus, a trade-off is not observed here because the inversion forces the model parameters to cover a more restricted range. In addition, the thermodynamic parameterization coupled with the top-down approach in which models are constructed (e.g., $d_{\text{lit}}/T_{\text{lit}}$ determine mantle temperature) acts to break the trade-off between various parameters that are treated as

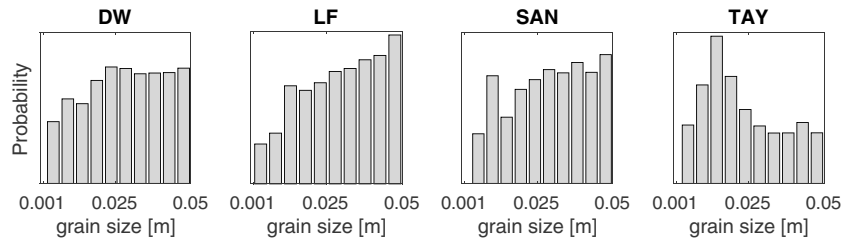


Figure 5. Sampled grain size distributions for the four main compositions DW, LF, SAN, and TAY (defined in Table 1).

being purely independent by Nimmo and Faul (2013) and restricts the parameter range even further. Finally, we also include $\bar{\rho}$ and l/MR^2 , which, relative to Nimmo and Faul (2013), exerts a strong independent control on density structure.

5.4. Attenuation

Inverted radial shear attenuation profiles $Q_{\mu}(r)$ for compositional model SAN are shown in Figure 6 at several periods: main period of the Phobos-induced tide (5.55 h), tidal period of the Sun (12.3 h), and at long (1 h) and short (1 s) seismic wave periods, respectively. Note that the $Q_{\mu}(r)$, k_2 , and Q are only constrained at the period of the Phobos-induced tide and unless otherwise stated, we refer to a period of 5.55 h. Also, only model results for SAN are shown here as the other compositions produce qualitatively similar results.

Because volatiles are abundant in the Martian crust, it is reasonable to believe that Q_{μ} in the crust and in the colder parts of the lithosphere (here fixed to 600) is less than on the Moon (~3,000–5,000) where cracks and pores filled with void prove extremely effective scatterers (Nakamura, 1977). In contrast, dissipation within

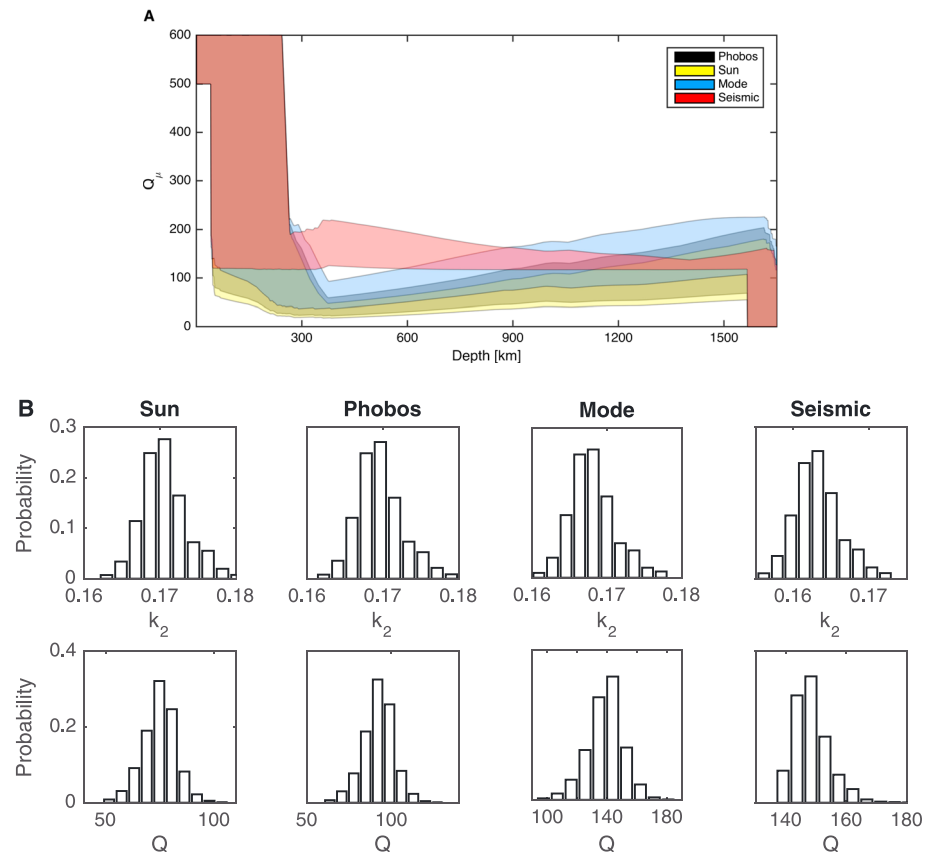


Figure 6. Attenuation profiles and tidal response at various periods in the tidal and seismic bands: Sun (12.3 h), Phobos (5.55 h), and long-period (“Mode”: 1 h) and short-period seismic waves (“Seismic”: 1 s). (a) Radial shear attenuation (Q_{μ}) models and (b) amplitude of tidal response (k_2) and global tidal dissipation (Q). Only model results for composition SAN are shown; the other compositions produce similar results.

the Martian mantle is large (small Q_{μ}) with a quasi-constant increase in Q_{μ} from 50–75 in the upper mantle to 150–200 in the lower mantle. $Q_{\mu}(r)$ is observed to follow the same trend at both longer (12.3 h) and shorter (1 h) periods but remains almost constant (~ 150) throughout most of the mantle at a period of 1 s.

The corresponding frequency-dependent tidal response is also shown in Figure 6. Since changes in shear wave speed (not shown) are negligible with relative variations of $<0.5\%$ in the period range 1–12.3 h, variations in k_2 are correspondingly small: k_2 (mean) varies from 0.17 (12.3 h) over 0.169 (5.55 h) to 0.168 (1 h). At similar periods Q (mean) varies from about ~ 75 over 91 to 132. The present trend for Q at longer periods (1–12.3 h) is observed to follow a power law behavior (Jackson & Faul, 2010) with a frequency-dependent exponent α in the range 0.25–0.4, that is, within the absorption band dissipation increases with increasing period and temperature. In contrast, in the seismic frequency band (1 s to 1 h), Q is observed to “level off,” indicative of small α (<0.1), i.e., Q becomes almost frequency-independent in line with terrestrial seismic experience. In the present case, the “leveling off” of Q at shorter periods is due to the effect of the “absorption peak” (cf. equation (13)) that Jackson and Faul (2010) identified in their laboratory experiments at relatively low temperatures.

Overall, the frequency-dependent tidal response in the period range 1–12.3 h found here agrees with the predictions of Zharkov and Gudkova (2005) who find global tidal dissipation factors of ~ 110 (Sun), ~ 125 (Phobos), and ~ 160 (1 h), respectively, using a power law creep function-based viscoelastic model with a frequency exponent of 0.15. The predictions of their model for Q (500–600) at seismic frequencies (1 s), however, diverge from the present results where a Q around 150–200 is found. Since their Q at 1 s is clearly too large, the authors consider a logarithmic creep law in the seismic frequency band instead, which implies a frequency-independent Q as a result of which a more reasonable value is obtained (Zharkov et al., 2017). In summary, to constrain the proper frequency-dependent behavior of Q , particularly at seismic periods, independent observations at different periods are needed, which should become available with the InSight mission.

The observation that the Martian mantle is dissipative could have a profound effect on seismic wave propagation within Mars. In particular, significant attenuation of both short-period body wave and long-period surface waves is possible and may hamper detection of distant (teleseismic) signals (see also discussion in Lognonné et al., 1996).

5.5. Core Parameters

Inverted core parameters (radius, composition sulfur content, and density) for the four main compositions, are shown in Figure 7 and summarized in Table 4. The results show remarkably similar core radii and compositions across the investigated compositional models with mean core radii and mean S contents (X_S) in the range 1,730–1,840 km and ~ 15 –18.5 wt% S, respectively.

Relative to the initial core compositions proposed by DW, LF, and TAY (Table 4), all the models require modification of the S content and total core mass in order to fit the geophysical observations. Importantly, and in spite of initial compositional differences between the four main models, inverted core parameters are seen to converge to the aforementioned common set of values. The estimates for the core obtained here are in good agreement with the recent estimates of Rivoldini et al. (2011), who employed a somewhat similar approach to determine the interior structure (inversion of k_2 , M , and I/MR^2) and obtained core radii and S contents of $1,794 \pm 65$ km and 16 ± 2 wt%, respectively.

The relatively large core sizes, however, imply that a lower mantle transition equivalent to the “660 km” seismic discontinuity is not extant inside Mars. CMB pressures attained here range from ~ 19 to 20 GPa, which is below that needed for the ringwoodite \rightarrow ferropericlasite+bridgmanite transition to occur (cf. Figure 1). A similar conclusion was also reached by Rivoldini et al. (2011).

Briefly, absence of a lower mantle has implications for the dynamical evolution of the planet: large cores inhibit the existence of a lower mantle layer as a result of which mantle convection is expected to encompass the entire mantle. Small cores, on the other hand, allow for a lower mantle layer that could form a dynamically separate unit and lead to decoupling of mantle and core (e.g., Ruedas et al., 2013a, 2013b; van Thienen et al., 2006), although disruption of grain size growth as material passes through the phase transition would tend to lower viscosity and hence increase convective vigor and therefore destabilize any initial separation. In contrast, absence of a lower mantle transition would favor continuous grain growth and lead to larger grain sizes and thus increased viscosity at the bottom of the mantle, which argues in favor of whole-mantle convection.

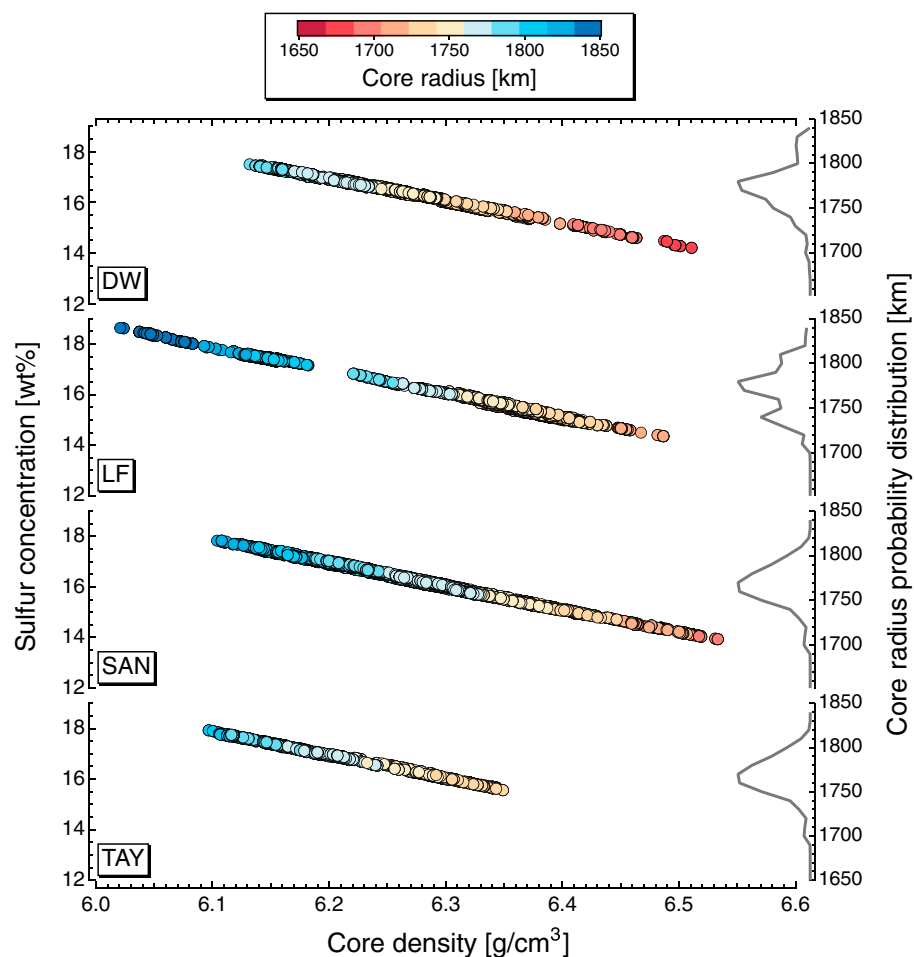


Figure 7. Sampled core properties: radius, sulfur content, and density for the four main compositions (defined in Table 1). The histograms on the right axis show the probability distributions of core radius for each of the main compositions.

Core compositions are modeled in the simplified system Fe-FeS because of a lack of more detailed geophysical models accounting for the effect of Ni on core properties. From a geochemical point of view, the core likely contains a significant amount of Ni, which can be estimated by assuming (1) that Ni is entirely incorporated into the core and (2) that bulk Mars has an atomic Fe/Ni ratio of 18. The latter assumption is based on a relatively constant Fe/Ni ratio among chondrites (ranging from 17.8 to 19.1; Wasson & Kallemeyn, 1988) but is also consistent with the estimates of DW and LF. Adjusting the core composition for the presence of Ni results in very similar solutions for all four models with a most probable core composition of ~ 75.5 – 80 wt% Fe, ~ 5 – 6 wt% Ni, and ~ 15 – 18.5 wt% S.

Relying on the experimental data of Stewart et al. (2007) of the system (Fe,Ni)-(Fe,Ni)S, the eutectic composition at the CMB pressures obtained here (~ 19 – 20 GPa) is around 17 wt% S and decreases to 14 wt% S with increasing pressure (40 GPa). Corresponding eutectic temperatures are below 1000°C at CMB pressures and only increase to 1100 – 1200°C at pressures of the inner core. In comparison, inverted model temperatures on the core side of the CMB are $>1600^\circ\text{C}$, which, together with the almost eutectic-like sulfur content with a mean around 15 – 18.5 wt%, suggests a fully liquid core at present in agreement with inferences made earlier (Rivoldini et al., 2011).

Mars' core is likely to undergo a complex core crystallization behavior in the future. Crystallization will start at the pressure at which the areotherm initially falls below the liquidus, which is expected to first occur in the upper part of the core close to the CMB on the Fe-rich side of the Fe-S eutectic (e.g., Dumberry & Rivoldini, 2015), consistent with the iron-rich "snowing core" hypothesis of (Stewart et al., 2007). Continued cooling

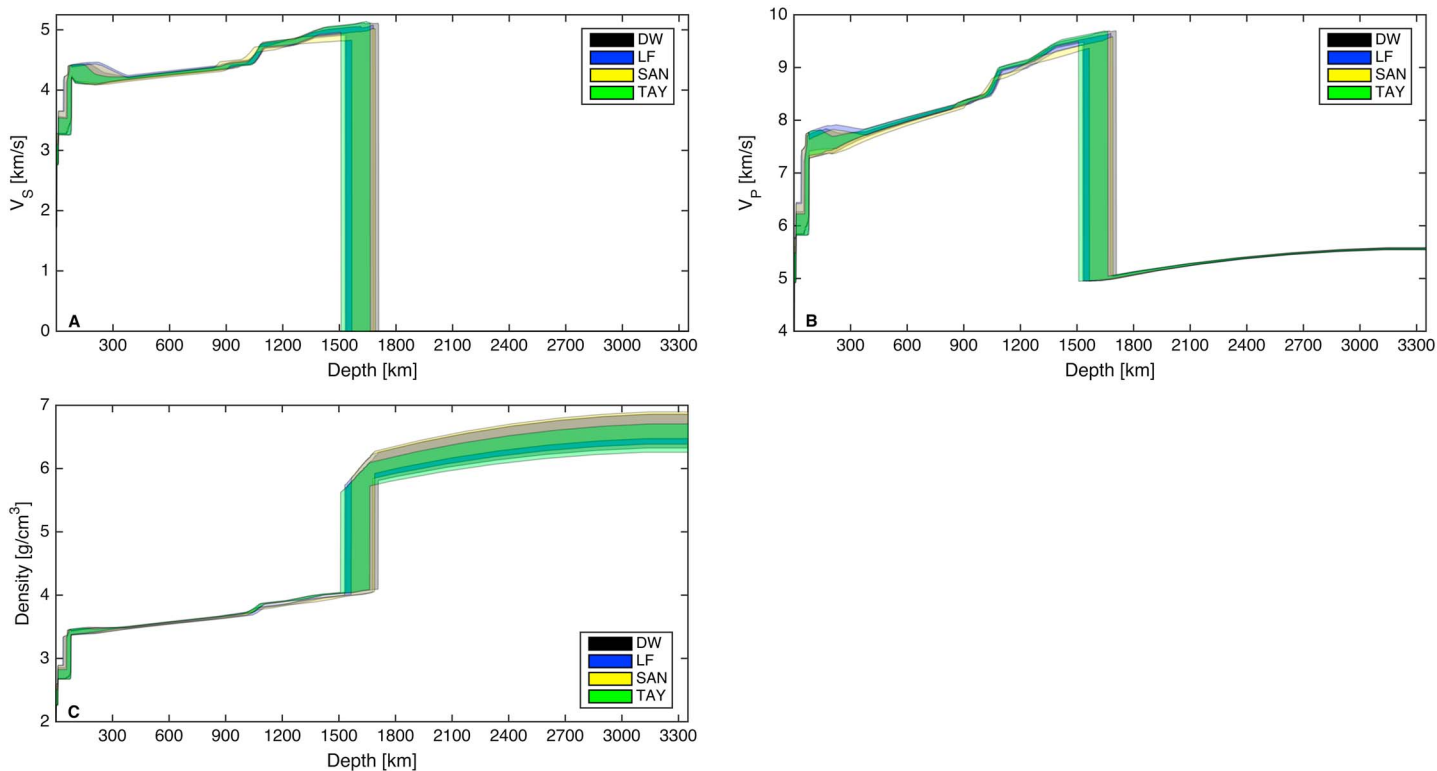


Figure 8. Sampled seismic velocity profiles for the four main compositions: (a) *S* wave speed, (b) *P* wave speed, and (c) density from the surface to the center of Mars. *S* wave models refer to a reference period of 1 s. See main text for details.

combined with the shift in eutectic composition toward Fe with increasing depth may result in a situation where the areotherm also intersects the liquidus on the S-rich side at higher pressure, causing cocrystallization of Fe₃S in the interior of the core (e.g., Hauck et al., 2006; Helffrich, 2017).

5.6. Implications for Bulk Composition

Constraints on the bulk composition of Mars derive from solving for core size and core sulfur content. The complementary bulk silicate Mars (BSM) component is defined by the input model compositions of DW, LF, SAN, and TAY (Table 1). These initial BSM compositions show some variability in absolute oxide concentrations and characteristic elemental ratios. The Mg number, for example, ranges between 0.751 (LF) and 0.728 (SAN) and varies only by ~3%. The atomic Mg/Si ratio, on the other hand, ranges from sub-CI chondritic (0.85) for SAN to near CI-chondritic (1.04) for TAY. With the present model setup, where we allow for a 10 wt% variation of each mantle oxide component (see Table 1), the BSM models are essentially indistinguishable. Since we are not inverting for the silicate composition of the mantle, we may express the inverted bulk composition simply by planetary bulk Fe/Si ratio (by weight and corrected for the presence of Ni in the core; see previous section), which varies between 1.66 (SAN) and 1.81 (TAY). Inverted bulk and bulk silicate Mars compositions are summarized in Table 4.

A simplification in our phase equilibrium calculations is that the “model mantle compositions” given in Table 1 are directly derived from the proposed BSM models and do not account for the extraction of the crust, i.e., that bulk silicate Mars is the compositional sum of crust and mantle. Subtracting mean crustal masses of average crustal composition (Table 1) from each mantle model shows that the residuals are within 10 wt% of their initial values, except for Na. The latter component is the most incompatible element and varies by up to 24 wt%. Because of its low absolute concentration, however, variations in Na have a negligible effect on mantle phase relations. Accordingly, crustal extraction can be considered implicit in the inversion.

5.7. Seismic Profiles

Of general interest in the context of the InSight mission are profiles of seismic velocity and density structure. These profiles are shown in Figure 8 and refer to seismic periods (1 s). As already seen in the thermal profiles (Figure 4), differences between the various models are relatively small. The models suggest the possible

presence of a lithospheric high-velocity lid followed by a low-velocity zone (LVZ). These features were noted previously by Nimmo and Faul (2013) and follow directly from the relatively strong temperature gradients that prevail in the conductive lithosphere. The effect of temperature on shear modulus relative to pressure inside Mars is stronger and therefore results in a shear wave velocity reduction with depth in the lithosphere. The effect of this on seismic wave propagation is discussed in detail by Zheng et al. (2015).

Models DW, LF, and TAY point to an olivine→wadsleyite transition at around $\sim 1,000$ – $1,050$ km depth and a secondary transition (wadsleyite→ringwoodite) at about $1,250$ – $1,300$ km depth. For model SAN the transitions occur ~ 50 km shallower in the mantle. On Earth, these transitions are relatively sharp and are detectable using seismic data in the form of mantle triplications, PP and SS precursors, and receiver functions (e.g., Lawrence & Shearer, 2006; Stähler et al., 2012; Tauzin et al., 2008). Inside Mars, however, the olivine→wadsleyite transition is not expected to be as sharp because of the protracted nature of the coexistence loop in comparison to Earth. This is likely going to complicate direct detection of mantle phase transitions by seismological means.

While seismic data will be acquired as part of the upcoming InSight mission to Mars, Figure 8 indicates that it is going to be difficult, based on seismic data alone, to discriminate between the compositional models investigated here. The same arguments concern determination of core size, which is otherwise detectable using normal modes (Okal & Anderson, 1978) or core-reflected (e.g., PcP and ScS) and core-refracted waves (e.g., PKP and SKS) (Helffrich, 2017). While seismic analyses in preparation for InSight have been and are currently undertaken (e.g., Böse et al., 2017; Bozdağ et al., 2017; Ceylan et al., 2017; Clinton et al., 2017; Goins & Lazarewicz, 1979; Khan et al., 2016; Larmat et al., 2008; Lognonné et al., 1996; Okal & Anderson, 1978; Panning et al., 2016; Solomon et al., 1991; Teanby & Wookey, 2011; Zharkov & Gudkova, 2014), we leave it for a future study to consider seismic predictions of the models proposed here in more detail.

6. Geodynamic Modeling

To provide an independent view on some of the geophysical predictions (e.g., grain size, thermal state, and lithospheric thickness), we performed a number of mantle convection simulations. For this purpose, we employ the convection code StagYY (Tackley, 2008) in 2-D spherical annulus geometry (Hernlund & Tackley, 2008). At this stage, we would like to note that it is not our purpose to accurately reproduce all geodynamical features of Mars (such as the activity related to the large volcanic provinces Tharsis and Elysium). Instead, the emphasis focusses on quantitatively reproducing the thermal profile (internal temperature) and average grain size obtained in the geophysical inversion, in addition to current crustal thickness estimates (e.g., Neumann et al., 2004; Wiczorek & Zuber, 2004).

An important constraint for the geodynamic simulations is the observation that most of Mars' crust is older than 3.7 Ga, although there is evidence for recent melting and volcanism (Carr & Head, 2010; Grott et al., 2013; Hauber et al., 2010; Neukum et al., 2004; Phillips et al., 2001; Solomon et al., 2005; Werner, 2009). As a consequence, "successful" models are expected to produce mafic crust mainly in the beginning of the simulations, although localized melt production is possible up until the present. Interestingly, the geophysically constrained internal temperatures are not too far below the solidus temperature (see Figure 4). This suggests that "localized" features such as a large plume below Tharsis (Harder & Christensen, 1996; Keller & Tackley, 2009; Roberts & Zhong, 2006; Šrámek & Zhong, 2010; Zhong, 2009; Zhong & Zuber, 2001) would allow for regional magmatism to occur without being widespread as observed on, for example, Io (Breuer & Moore, 2007) and Venus (Ivanov & Head, 2013). In the simulations performed here, we neglect the implications of a giant impact as a means of forming most of the north-south crustal dichotomy (Golabek et al., 2011; Marinova et al., 2008; Nimmo et al., 2008; Reese et al., 2010). As a result, the amount of mafic crust that forms is likely to be underestimated.

6.1. Crustal Production and Grain Size Evolution

For the simulations, we solve the equations of compressible thermochemical convection, that is, Stokes, heat, and continuity equations employing the marker in cell method for the advection of rock composition, temperature, and grain size using the convection code StagYY (Tackley, 2008). Here only a brief summary is given. Details are provided in Appendix B.

When temperature exceeds the mantle solidus, partial melting ensues. The basaltic melt produced from the mixed mantle is transported toward the surface by both intrusive (50%) and extrusive (50%) magmatism,

as described in Rozel et al. (2017). The solid residue is harzburgitic in composition (forming the depleted mantle) and will remain solid as the compositionally dependent solidus temperature increases (Maaløe, 2004). Heat-producing elements preferentially partition into the melt, implying that the mafic crust deposited at the surface is $1/D_p$ times more radiogenic than the depleted residue where D_p is the partition coefficient for radiogenic heat-producing elements. For the partitioning of heat-producing elements between the mantle and crust we use the approach described in Xie and Tackley (2004). Our simulations show that D_p is an important parameter as it controls the effective internal heat production in Mars' mantle, which directly influences the internal temperature through melting and crustal production. Experimentally determined values for D_p of radiogenic elements are of the order of 0.001 (Hart & Dunn, 1993; Hauri et al., 1994).

In the simulations performed here, we assume a homogeneous temperature-, pressure-, and grain size-dependent rheological equation based on diffusion creep (Hirth & Kohlstedt, 2013) over the entire computational domain

$$\eta(P, T, d_{\text{grain}}) = \eta_0 \left(\frac{d_{\text{grain}}}{d_{\text{ref}}} \right)^3 \exp \left(\frac{E + PV}{RT} - \frac{E}{RT_{\text{ref}}} \right), \quad (23)$$

where η_0 and d_{ref} are reference viscosity and grain size (1 mm), respectively, E and V are activation energy (375 kJ/mol) and activation volume (6 cm³/mol), respectively, T_{ref} is reference temperature (1326°C), and R is the universal gas constant. This expression for η is similar to equation (14) with $\eta = \tau\mu$, but the latter applies to timescales on the order of Phobos' orbital period (hours), whereas here timescales refer to the evolution of Mars (Gyr). To reproduce geodynamically the geophysically inferred properties, we test various reference viscosities in the range 10^{18} – 10^{21} Pa s.

Grain size evolution and heat-producing element partitioning are interrelated as grain growth is strongly temperature dependent, in that internal heating tends to increase grain size, while simultaneously producing mafic crust. Yet, magmatism depletes the mantle, that is, decreases internal heating, and limits any increase in potential temperature. Consequently, it is reasonable to assume that the evolution of Mars' internal temperature and average grain size are governed by depletion in heat sources due to melting and magmatism.

To avoid numerical diffusion, grain size evolution is computed on the Lagrangian markers advected by the flow. We use a simple grain growth equation and neglect dynamic recrystallization since grain size reduction terms are negligible due to the small stresses in the Martian mantle

$$\frac{D}{Dt} d_{\text{grain}}^p = k_0 \exp \left(-\frac{E_d}{RT} \right), \quad (24)$$

where k_0 , p , and E_d are experimentally determined constants. In line with arguments made earlier (section 5.3), we use a single grain growth law for the entire mantle. Grain growth parameters are difficult to determine experimentally as laboratory experiments can only be run for a limited amount of time, far less than the scale on which geological processes occur. To fully investigate the effects of grain size evolution, we consider four different growth parameters. First, following Yamazaki et al. (2005), we chose $p = 4.5$, $k_0 = 3.9811 \cdot 10^6 \mu\text{m}^{4.5}/\text{s}$ and $E_d = 414$ kJ/mol. Second, to model the effect of faster kinetics, we consider three additional growth laws within the range of the measurements of Hiraga et al. (2010) for which $p = 5$, $k_0 = 1.75 \cdot 10^8$, $k_0 = 1.75 \cdot 10^9$, and $k_0 = 1.75 \cdot 10^{10}$, respectively. As discussed earlier, midmantle phase transitions (olivine→wadsleyite and wadsleyite→ringwoodite) are not expected to affect grain size (see also Solomatov & Reese, 2008).

The initial state is characterized by a potential temperature of 1326°C and a homogeneous grain size of 100 μm . The mantle is a mixture of 15% eclogite and 85% harzburgite, and we impose a 20 km preexisting basaltic crust at the surface. Radiogenic heating of mixed mantle is initially equal to $2.3 \cdot 10^{-11}$ W/kg and decreases exponentially throughout time with a half-life of 2.43 Gyr (Nakagawa & Tackley, 2005). We operate with an initial core temperature of 2226°C and take into account self-consistent core cooling using the heat flux at the CMB. Core radius is fixed to ~ 1700 km.

6.2. Geodynamical Results

Figure 9 shows final profiles of temperature, viscosity, and grain size after 4.5 Gyr of evolution. Temperature and grain size profiles are strongly correlated, as expected, since the final grain size represents an integral of the thermal history; a hot mantle results in a larger grain size. Viscosity, on the other hand, does not correlate with temperature nor grain size, since these parameters compete in the rheological equation (equation (23)).

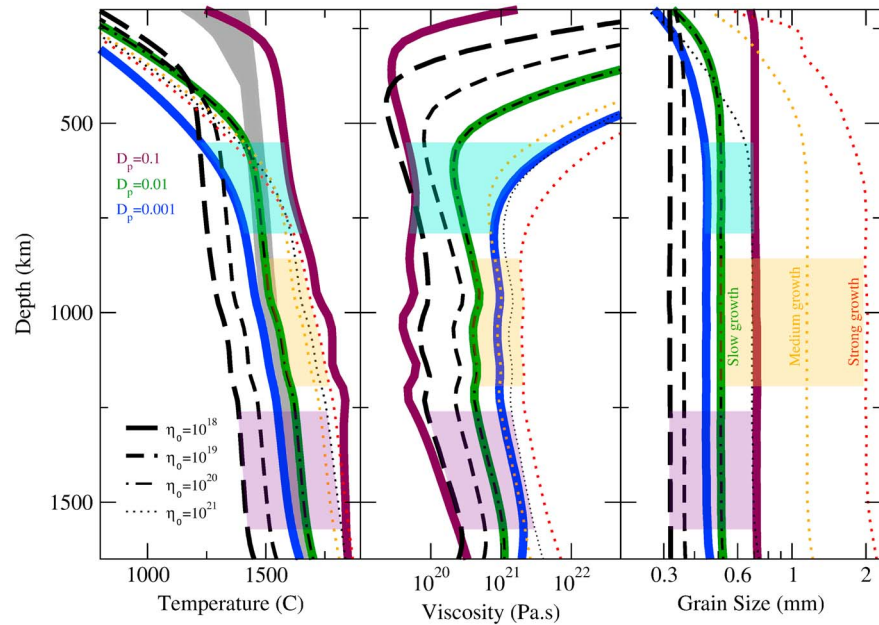


Figure 9. Temperature (a), viscosity (b), and grain size (c) profiles after 4.5 Gyr of evolution for various initial values of radioactive element partition coefficients (D_p), grain growth prefactors k_0 , and reference viscosities (η_0 in Pa s). Dark gray shaded region in (a) shows the geophysically derived thermal profiles for the DW composition (cf. Figure 4). Shaded regions show impact of variations in D_p (turquoise), k_0 (orange), and η_0 (purple).

For comparison, geophysically inverted thermal profiles are also shown (gray envelope). From the results we observe the following trends: inefficient partitioning of heat-producing elements (high D_p) results in larger internal temperatures and thinner lithospheres, whereas low reference viscosities tend to better cool the mantle and result in thinner lithospheres. Also, strong grain growth tends to increase the internal temperature and thicken the lithosphere.

To provide a more quantitative expression for these trends, we used the viscosity profiles to detect the lithosphere-asthenosphere boundary (LAB). The latter was defined as being located where the viscosity is 20% higher than the smallest viscosity value found below the lithosphere. From this, the following scaling laws for lithospheric thickness and temperature (generated in all simulations) were obtained

$$\frac{d_{lit}(km)}{500} = 1.278 \left(\frac{\ln D_p}{A} \right)^{0.806} \left(\frac{\eta_0}{\eta'} \right)^{0.099} \left(\frac{\ln k_0}{B} \right)^{1.208} \quad (25)$$

$$\frac{T_{lit}(K)}{1600} = 1.106 \left(\frac{\ln D_p}{A} \right)^{-0.071} \left(\frac{\eta_0}{\eta'} \right)^{0.031} \left(\frac{\ln k_0}{B} \right)^{0.334}, \quad (26)$$

where d_{lit} and T_{lit} are in units of kilometers and kelvin, respectively, and $A = \ln 0.01$, $B = \ln 10^9$, and $\eta' = 10^{20}$ Pa s throughout. Lithosphere thickness has been limited to 1,000 km in these scaling laws. To fit all cases with a single scaling law using a common k_0 , we modified the k_0 from the simulations with a p exponent of 4.5 as follows. We sought the k_0 that produces the same grain size after 4.5 Gyr evolution for an exponent $p=5$ and a temperature $T=1500^\circ\text{C}$. This occurs for a k_0 of $7.652 \cdot 10^7$.

Figure 9 also shows that the internal viscosity and grain size (second and third panels) depend on D_p , k_0 , and η_0 . At a depth of 1,000 km, the scaling laws for internal viscosity η_{int} and grain size d_{grain} were found to be

$$\frac{\eta_{int}}{10^{20}} = 8.86 \left(\frac{\ln D_p}{A} \right)^{2.876} \left(\frac{\eta_0}{\eta'} \right)^{0.526} \left(\frac{k_0}{10^9} \right)^{0.334} \quad (27)$$

$$\frac{d_{grain}}{500} = 1.914 \left(\frac{\ln D_p}{A} \right)^{0.112} \left(\frac{\eta_0}{\eta'} \right)^{0.085} \left(\frac{k_0}{10^9} \right)^{0.233}, \quad (28)$$

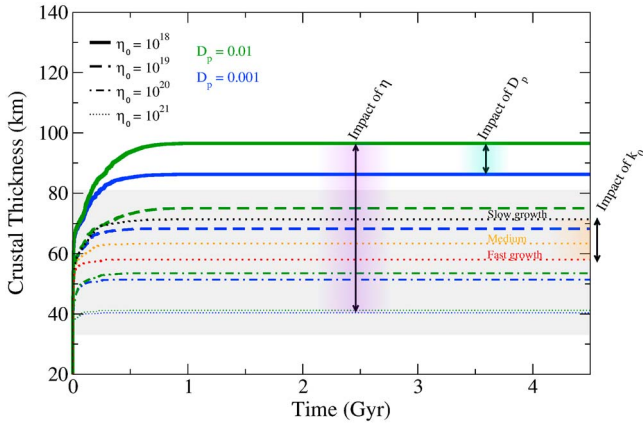


Figure 10. Amount of crust (in kilometer thickness) erupted to the surface through time for various radioactive element partition coefficients (D_p), grain growth prefactors k_0 , and reference viscosities (η_0 in Pa s). For comparison, gray shaded area indicates the range of current average crustal thickness estimate of Wicczorek and Zuber (2004). Color-shaded regions show impact of variations in D_p (turquoise), k_0 (orange), and η_0 (purple).

where η_{int} and d_{grain} are in units of Pa s and micrometers, respectively. These relations indicate that both viscosity and grain size increase with increasing D_p , k_0 , and η_0 . Grain sizes larger than 1 mm, consistent with what was found in the geophysical inversion, are observed in the simulations involving medium-to-large grain growth (Figure 9).

The present-day average surface heat flux (Q_{HF}) obtained in our simulations ranges from 15 to 25 mW/m². This is in good agreement with the estimates derived by Plesa et al. (2016) where mean surface heat fluxes in the range 23–27 mW/m² were obtained. An important observation here is that partitioning of heat-producing elements, small grain growth, and a low viscosity tend to slightly increase the heat flux, as summarized by the scaling law:

$$\frac{Q_{HF}}{25} = 0.715 \left(\frac{\ln D_p}{A} \right)^{-0.378} \left(\frac{\eta_0}{\eta'} \right)^{-0.0137} \left(\frac{\ln k_0}{B} \right)^{-0.155}, \quad (29)$$

where the heat flux is expressed in mW/m². The above five scaling laws are illustrated in Figure B1 in Appendix B.

Finally, Figure 9 shows that the geophysically derived temperature profiles in the lithosphere (gray shaded area) are not easily reproduced. Mantle

temperatures are fit for a large variety of parameters, but lithosphere thickness is generally >300 km, that is, toward the upper end of the geophysical results. A thinner lithosphere is only obtained in the case of low viscosity and large D_p . In the context of the geophysically determined grain sizes, Figure 9 shows that grain sizes greater than 1 mm are only really possible in the case of relatively strong grain growth, which nonetheless remains much slower than pure olivine growth in the absence of Zener pinning.

Figure 10 shows that large D_p values tend to increase the thickness of the crust. In particular, inefficient partitioning of heat-producing elements ($D_p = 0.1$), irrespective of the value of η_0 , can be ruled out because mantle temperatures are too high by several hundred degrees relative to the inverted profiles and so is crustal production ($\gg 200$ km, not shown in Figure 10). Summarizing the results, we find that present-day crustal thickness follows a scaling relationship of the form (see Figure B1)

$$\frac{d_{moho}}{80} = 0.569 \left(\frac{\ln D_p}{A} - 0.500 \right)^{-0.182} \left(\frac{\eta_0}{\eta'} \right)^{-0.113} \left(\frac{\ln k_0}{B} \right)^{-0.913}. \quad (30)$$

Thus, the preferred values of D_p , k_0 , and η_0 that are consistent with the geophysical predictions seem to be $0.01 < D_p < 0.1$, a large k_0 , and $10^{18} < \eta_0 < 10^{20}$. The geodynamical results (Figures 9 and 10) supporting the scaling laws (equations (25)–(29)) are summarized in Table 5.

Table 5
Summary of Geodynamic Modeling Results Supporting the Scaling Laws (Equations (25)–(29))

η_0 (Pa s)	D_p	d_{lit} (km)	T_{lit} (°C)	d_{grain} (μ m)	η_{int} (Pa s)	Q_{HF} (mW/m ²)	d_{moho} (km)	k_0 (m ^p /s)	p
10^{18}	10^{-3}	479	1152	291	$1.8 \cdot 10^{20}$	16.8	86	$3.98 \cdot 10^6$	4.5
10^{18}	10^{-3}	552	1222	610	$4.1 \cdot 10^{20}$	16.7	77	$1.75 \cdot 10^9$	5
10^{18}	10^{-3}	500	1166	356	$2.5 \cdot 10^{20}$	16.8	85	$1.75 \cdot 10^8$	5
10^{18}	10^{-3}	618	1288	1087	$6.3 \cdot 10^{20}$	16.5	70	$1.75 \cdot 10^{10}$	5
10^{19}	10^{-3}	579	1240	335	$4.8 \cdot 10^{20}$	16.6	68	$3.98 \cdot 10^6$	4.5
10^{19}	10^{-3}	675	1342	766	$8.7 \cdot 10^{20}$	16.3	61	$1.75 \cdot 10^9$	5
10^{19}	10^{-3}	599	1264	420	$5.5 \cdot 10^{20}$	16.6	65	$1.75 \cdot 10^8$	5
10^{19}	10^{-3}	795	1421	1380	$1.6 \cdot 10^{21}$	16.0	56	$1.75 \cdot 10^{10}$	5
10^{20}	10^{-3}	716	1378	447	$9.2 \cdot 10^{20}$	16.1	51	$3.98 \cdot 10^6$	4.5
10^{20}	10^{-3}	950	1518	941	$2.5 \cdot 10^{21}$	15.7	48	$1.75 \cdot 10^9$	5
10^{20}	10^{-3}	756	1403	539	$1.1 \cdot 10^{21}$	16.0	49	$1.75 \cdot 10^8$	5

Table 5 (continued)

η_0 (Pa s)	D_p	d_{lit} (km)	T_{lit} (°C)	d_{grain} (μm)	η_{int} (Pa s)	Q_{HF} (mW/m ²)	d_{moho} (km)	k_0 (m ^p /s)	p
10 ²⁰	10 ⁻³	997	1555	1525	8.2 · 10 ²¹	15.5	43	1.75 · 10 ¹⁰	5
10 ²¹	10 ⁻³	979	1540	536	3.9 · 10 ²¹	15.5	40	3.98 · 10 ⁶	4.5
10 ²¹	10 ⁻³	1008	1565	965	1.9 · 10 ²²	15.3	37	1.75 · 10 ⁹	5
10 ²¹	10 ⁻³	988	1550	610	5.3 · 10 ²¹	15.5	39	1.75 · 10 ⁸	5
10 ²¹	10 ⁻³	1013	1538	1283	7.2 · 10 ²²	15.1	33	1.75 · 10 ¹⁰	5
10 ¹⁸	10 ⁻²	399	1178	317	8.1 · 10 ¹⁹	18.8	96	3.98 · 10 ⁶	4.5
10 ¹⁸	10 ⁻²	454	1252	657	1.9 · 10 ²⁰	18.5	84	1.75 · 10 ⁹	5
10 ¹⁸	10 ⁻²	411	1191	380	1.2 · 10 ²⁰	18.8	93	1.75 · 10 ⁸	5
10 ¹⁸	10 ⁻²	502	1326	1202	3.0 · 10 ²⁰	18.3	75	1.75 · 10 ¹⁰	5
10 ¹⁹	10 ⁻²	478	1269	362	2.4 · 10 ²⁰	18.4	74	3.98 · 10 ⁶	4.5
10 ¹⁹	10 ⁻²	534	1384	866	3.8 · 10 ²⁰	18.0	63	1.75 · 10 ⁹	5
10 ¹⁹	10 ⁻²	489	1301	458	2.6 · 10 ²⁰	18.4	71	1.75 · 10 ⁸	5
10 ¹⁹	10 ⁻²	613	1472	1634	6.2 · 10 ²⁰	17.4	58	1.75 · 10 ¹⁰	5
10 ²⁰	10 ⁻²	554	1416	512	4.4 · 10 ²⁰	17.8	53	3.98 · 10 ⁶	4.5
10 ²⁰	10 ⁻²	655	1527	1149	9.5 · 10 ²⁰	17.0	49	1.75 · 10 ⁹	5
10 ²⁰	10 ⁻²	570	1448	628	4.6 · 10 ²⁰	17.6	51	1.75 · 10 ⁸	5
10 ²⁰	10 ⁻²	784	1614	2030	2.1 · 10 ²¹	16.5	44	1.75 · 10 ¹⁰	5
10 ²¹	10 ⁻²	703	1560	689	1.4 · 10 ²¹	16.7	41	3.98 · 10 ⁶	4.5
10 ²¹	10 ⁻²	853	1664	1313	3.5 · 10 ²¹	16.1	38	1.75 · 10 ⁹	5
10 ²¹	10 ⁻²	734	1583	797	1.5 · 10 ²¹	16.6	40	1.75 · 10 ⁸	5
10 ²¹	10 ⁻²	896	1715	2226	1.2 · 10 ²²	15.8	33	1.75 · 10 ¹⁰	5
10 ¹⁹	10 ⁻¹	212	1432	677	1.0 · 10 ¹⁹	26.7	368	3.98 · 10 ⁶	4.5
10 ¹⁹	10 ⁻¹	283	1480	1209	2.9 · 10 ¹⁹	23.6	239	1.75 · 10 ⁹	5
10 ¹⁹	10 ⁻¹	332	1550	2079	8.2 · 10 ¹⁹	23.3	221	1.75 · 10 ¹⁰	5
10 ²⁰	10 ⁻¹	303	1507	714	4.3 · 10 ¹⁹	23.4	230	3.98 · 10 ⁶	4.5
10 ²⁰	10 ⁻¹	374	1600	1398	2.1 · 10 ²⁰	23.4	208	1.75 · 10 ⁹	5
10 ²⁰	10 ⁻¹	315	1525	808	6.4 · 10 ¹⁹	23.4	226	1.75 · 10 ⁸	5
10 ²⁰	10 ⁻¹	441	1672	2533	6.4 · 10 ²⁰	23.4	186	1.75 · 10 ¹⁰	5
10 ²¹	10 ⁻¹	406	1633	855	4.0 · 10 ²⁰	23.5	192	3.98 · 10 ⁶	4.5
10 ²¹	10 ⁻¹	481	1717	1741	1.3 · 10 ²¹	23.7	159	1.75 · 10 ⁹	5
10 ²¹	10 ⁻¹	420	1650	978	5.1 · 10 ²⁰	23.5	189	1.75 · 10 ⁸	5
10 ²¹	10 ⁻¹	556	1776	3104	3.7 · 10 ²¹	23.9	139	1.75 · 10 ¹⁰	5

Note. d_{grain} and η_{int} refer to a reference depth of 1,000 km, whereas d_{moho} represents the final crustal thickness after 4.5 Gy of evolution. Parameters are defined in Table 3 and in section 6.

While a D_p in the range 0.01–0.1 is found to be preferable, this particular scenario nevertheless tends to generate too much crust and therefore larger crustal thicknesses than permitted by current observations. However, as a word of caution, we should note that several aspects currently limit the accuracy of the estimated crustal production. First, crustal production is intimately related to the solidus temperature profile of Mars which is uncertain. Second, crustal recycling is somewhat underestimated in our models as we imposed 50% of volcanism and 50% of plutonism. Higher plutonic efficiency, for example, would lead to more efficient recycling (Rozel et al., 2017) and thereby allow for a thinner present-day crust. These issues will have to be investigated in more detail in the future.

7. Summary and Conclusion

We have shown that a grain size and frequency-dependent viscoelastic model (extended Burgers rheology) based on laboratory deformation of melt-free polycrystalline olivine is capable of matching a set of geophysical observations for Mars. In particular, we have shown that mantle melting is not required to reproduce

the relatively dissipative Martian interior. Starting from a set of initial geochemically based bulk Martian compositions, we find strong evidence for a relatively large (radius~1,730–1,840 km) Fe core containing 15–18.5 wt% S that appears to be entirely liquid at present given current constraints, data, and modeling assumptions. The results preclude the presence of a solid inner core on account of the determined core S content, which is close to the eutectic composition. The model geotherms obtained here remain below the present-day dry Martian solidus inferred by Kiefer et al. (2015) and indicate CMB temperatures around 1560–1660°C. From the determined core size and CMB pressure and temperature, the presence of a lower mantle transition, equivalent of the 660 km seismic discontinuity in the Earth, seems unlikely. The bulk Martian compositions derived here are generally chondritic with a Fe/Si (weight ratio) of 1.66–1.81. Grain size estimates range from 1 to 50 mm but are >0.5 mm and within the range observed on Earth.

Following this, we performed a number of thermochemical evolution simulations with the purpose of fitting the geophysically derived results (specifically mantle geotherm, lithospheric thickness, and grain size). This served to show that the inversion results can be used in tandem with geodynamic simulations to identify plausible geodynamic scenarios and parameters. For a reasonable set of radioactive element partition coefficients between crust and mantle around 0.01–0.1 and reference viscosities (10^{18} – 10^{20} Pa s), the geodynamic models, based on 2-D models and covering 4.5 Ga of Martian history, were generally able to reproduce current areotherms, crustal thickness, and grain size, but, in part only, lithospheric thickness. The geodynamic models also predict a present-day mean surface heat flow between 15 and 25 mW/m², in excellent agreement with the recent heat flow estimates by (Plesa et al., 2016).

We should emphasize that the point of the geodynamical simulations was not to accurately reproduce the dynamical evolution of Mars but rather (1) to provide first-order insights on the long-term evolution (~4.5 Gyr) in terms of a few crucial parameters such as crustal production, mantle temperature, and grain size growth and (2) to see if these can be varied within reasonable bounds while simultaneously fitting the present-day geophysical predictions obtained here.

Being anhydrous and melt-free, the models constructed here are end-member cases in that presence of, for example, water would lower the solidus (e.g., Pommier et al., 2012), produce melt, and increase dissipation, which would have to be offset by an overall decrease in mantle temperature. The thermal evolution of Mars depends crucially on mantle viscosity, which is also determined by conditions of temperature, pressure, and water content. Even if present at small levels (tens of ppm), water can lead to a reduction of effective viscosity and Q , thereby enhancing dissipation (Hirth & Kohlstedt, 1996; Karato, 2013; Karato & Jung, 1998; Mei & Kohlstedt, 2000). As discussed by Filiberto et al. (2016), presence of 0.02 wt% water in the mantle source region would lower viscosity by a factor of 36 relative to a nominally dry (≤ 10 ppm water) mantle with an associated significant increase in convective vigor as observed in various dynamical evolution studies (e.g., Hauck & Phillips, 2002; Li & Kiefer, 2007; Morschhauser et al., 2011; Ogawa & Yanagisawa, 2012; Ruedas et al., 2013b). The combined effect of this would be to lower the mantle geotherm below what has been obtained here. Accordingly, the present mantle geotherms represent upper bounds.

Although water in some shergottite magmas has been observed (McCubbin et al., 2012), the present-day water content of the Martian mantle is not well constrained. It likely contains less water than Earth with a probable value of around 300 ppm (Taylor, 2013). This estimate assumes no water loss during or after accretion due to impact heating, chemical reactions, and magma ocean crystallization (Elkins-Tanton et al., 2005; Wänke & Dreibus, 1994). For now, the effect of water needs to be better quantified and understood before it can be modeled properly. In addition, current lack of thermodynamic data accounting for the influence of water on mantle phase equilibria further prohibits quantitative modeling.

Presence of melt very much mimics the effect of water, that is, lowers Q and increases dissipation. While there is some evidence for magmatic activity that might have occurred until relatively recently (e.g., Neukum et al., 2004; Niles et al., 2010), Mars is unlikely to be molten on the global scale at present. Even if localized pockets or regions inside Mars may have remained molten up until the present, these are unlikely to affect global dissipation.

What can be argued based on the results here and those of Nimmo and Faul (2013) is that laboratory-based viscoelastic dissipation models do not require melt to fit current observations. The effect of a small melt fraction on dissipation has been studied in the laboratory (e.g., Faul et al., 2004; McCarthy & Takei, 2011; Takei, 2017). Melt acts to enhance dissipation and render it essentially frequency independent across the seismic

frequency band (Faul et al., 2004). However, modeling its influence presents, on a par with water, an equally challenging problem that will be left for a future study.

In this context, earlier studies based on viscoelastic models (e.g., Bills et al., 2005; Castillo-Rogez & Banerdt, 2013) that relied on different rheologies (Maxwell and Andrade) found mantle viscosities around 10^{14} – 10^{16} Pa s that appear to be inconsistent with current estimates of Earth's mantle viscosity ($\sim 10^{19}$ – 10^{21} Pa s). This suggested that either Mars does not behave as a Maxwell body or that a significant amount of partial melt is needed to lower the viscosity to the aforementioned values. The latter possibility has gained in strength in the case of the Moon, where evidence in support of partial melt in the deep lunar interior has steadily accumulated (e.g., Efroimsky, 2012a, 2012b; Harada et al., 2014; Khan et al., 2014; Weber et al., 2011; Williams & Boggs, 2015; Williams et al., 2001), although Nimmo et al. (2012) find that melt is not strictly required to match the observations with the caveat that the frequency dependence of Q (i.e., α) at tidal periods is opposite in sign to what has been observed through lunar laser ranging (e.g., Williams et al., 2014). As pointed out by Efroimsky (2012a), though, the lunar laser ranging-based observation of a negative α (i.e., $Q \sim \omega^\alpha$ instead of the common case where $Q \sim \omega^{-\alpha}$) is entirely in accordance with a low-viscosity attenuating region in the lunar interior. Employing a homogeneous incompressible spherical model of the Moon, Efroimsky (2012a) and Efroimsky (2012b) showed that the apparent decrease of k_2/Q with period observed through lunar laser ranging could be explained with a function equivalent to a single relaxation time model. Using a viscosity around ($\sim 10^{15}$ Pa s), k_2/Q was shown to peak in the tidal band in the vicinity of the tidal periods (see, e.g., Figure 1 in Efroimsky, 2015). We leave it for a future study to consider the impact of different types of rheological models in the context of the inverse problem posited here.

The present approach is not fully self-consistent in that only a single mineral (olivine) and a single composition (Fo_{90}) has had its viscoelastic behavior characterized; nonetheless, Nimmo and Faul (2013) argue that the errors introduced by focusing exclusively on Fo_{90} olivine are likely to be small, since the behavior of olivine is believed to be broadly representative of the viscoelastic behavior of the upper mantle. Compositional effects will mainly influence the unrelaxed modulus (I. Jackson, personal communication, 2014). Based on a compilation of existing data, Karato (2013) similarly argues that addition of orthopyroxene to olivine has little effect on anelasticity. In line herewith, and because olivine is the dominant mineral ($\sim 60\%$ by volume) throughout most of the Martian mantle, neglect of the contribution from other phases is expected to less likely result in significant changes. In view of the different Mg#s of Earth and Mars, a possible exception is the iron content that could potentially change the dissipative properties of olivine (Zhao et al., 2009). We leave it for a future treatment, based on a new and expanded experimental database, to consider these effects in more detail. Also, while this study is based on the most appropriate experimental constraints available, their use involves an extrapolation beyond the available experimental frequencies as well as an extrapolation in grain size. Further experiments closer to the Martian parameter space we explore would be valuable future work.

In spite of these caveats, the approach outlined here is capable of making significant predictions (summarized in Table 4) that provide many quantitative insights. Moreover, the study proposed here will help quantify additional future requirements—from the acquisition of new experimental data to modeling aspects—that will be in need of further attention to extend the predictions to increasingly complex models.

Last, but not least, the predictions made here can ultimately be tested with the upcoming InSight mission that will perform the first in situ measurements of the interior of Mars through the acquisition of seismic, heat flow, and geodetic data:

1. Analysis of the seismic data to be returned from the SEIS experiment (Lognonné et al., 2012) on InSight will rely on more “classical” global seismology techniques in the form of traveltimes tables for various seismic phases, surface wave dispersion, receiver functions, normal modes, and waveforms (e.g., Okal & Anderson, 1978; Panning et al., 2016; Zheng et al., 2015). These data will shed light on the interior physical structure of crust, mantle, and core, including velocity gradients and discontinuities associated with mineral phase transitions and/or chemical boundaries. Moreover, the data will help constrain Martian seismicity and tectonism and, not least, meteorite impact rates (e.g., Golombek et al., 1992; Knapmeyer et al., 2006; Teanby & Wookey, 2011).
2. On a par with the importance of acquiring seismic data, measuring heat flow with the heat flow probe (HP³) onboard InSight (Spohn et al., 2014) cannot be overestimated, because it will allow for an independent means of distinguishing between the various bulk compositional models. Specifically, by combining the heat flow measurement with numerical estimates of the Urey ratio (e.g., Plesa et al., 2015), it will be

possible to constrain the heat production rate and thus bulk abundance of heat-producing elements in the interior of Mars. Comparison of the latter with the proposed compositional models for Mars provides the necessary tool.

3. In the context of improving estimates of core structure, the RISE (Rotation and Interior Structure Experiment) instrument on board InSight will prove important (e.g., Folkner et al., 2012; van Hoolst et al., 2012). Through precise radio tracking of the landed spacecraft, RISE will be able to measure the precession rate and through it allow for a more accurate estimation of the polar moment of inertia. In particular, for a fluid Martian core, the nutation of the spin axis can be resonantly amplified and allow for an independent estimation of the polar moment of inertia of the core. From precise estimation of the period of the free core nutation, the moment of inertia of the core can be estimated. These parameters are crucially sensitive to core size, shape, and state. RISE observations over a Martian year should enable a clear detection of the nutation signature and thus core parameters.

These data sets, individually and in combination, will prove to be the Rosetta stone for unraveling the thermochemical structure and evolution of Mars.

Appendix A: Thermoelastic Properties of the Core

The thermoelastic properties of the liquid core alloy as a function of pressure (P) and temperature (T) are calculated following Dumberry and Rivoldini (2015), with the exception of equation (A12), and are contained here for completeness. In this approach, it is assumed that the properties of the alloy can be calculated from the thermoelastic properties of liquid Fe and liquid Fe-10 wt% S (hereafter referred to as Fe and FeS₁₀) and that both components mix ideally. Based on this, the molar volume V of the solution is given by

$$V = \sum_{i=1}^2 \chi_i V_i, \quad (\text{A1})$$

where $\chi_1 = 1 - \chi_2$ is the molar fraction of Fe and χ_2 the molar fraction of FeS₁₀. The molar concentration of sulfur in FeS₁₀ is related to the weight fraction of sulfur in the solution, X_S , by

$$\chi_2 = \frac{X_S}{\chi_{S_{10}}} \frac{M_{\text{Fe}}}{M_S(1 - X_S) + M_{\text{Fe}}X_S}, \quad (\text{A2})$$

where $M_{\text{Fe}} = 55.845$ g/mol and $M_S = 32.065$ g/mol are the molar masses of iron and sulfur, respectively, and $\chi_{S_{10}} = 0.162137$ is the atomic fraction of sulfur in FeS₁₀.

The thermal expansivity α , isothermal bulk modulus K_T , and pressure derivative K'_T of the solution can be derived from equation (A1) through the application of standard thermodynamic relations

$$\alpha V = \sum_{i=1}^2 \chi_i \alpha_i V_i, \quad (\text{A3})$$

$$\frac{V}{K_T} = \sum_{i=1}^2 \chi_i \frac{V_i}{K_{T,i}}, \quad K'_T = -1 + \frac{K_T^2}{V} \sum_{i=1}^2 \chi_i \frac{V_i}{K_{T,i}} (1 + K'_{T,i}). \quad (\text{A4})$$

In order to compute the isentropic temperature gradient in the core (equation (17)), the adiabatic bulk modulus K_S and the Grüneisen parameter γ are also required. K_S is related to the isothermal bulk modulus K_T by the following relation (e.g., Poirier, 2000):

$$K_S = K_T (1 + \alpha \gamma T). \quad (\text{A5})$$

To compute γ , we rely on the formulation of Vashchenko and Zubarev (e.g., Poirier, 2000):

$$\gamma = \frac{\frac{1}{2}K'_T - \frac{5}{6} + \frac{2}{9}PK_T^{-1}}{1 - \frac{4}{3}PK_{T-1}}. \quad (\text{A6})$$

To compute thermoelastic properties for each component at P and T , we first perform an isothermal compression from the reference conditions (P_0, T_0) to (P, T_0), followed by isobaric heating to (P, T). For the isothermal

Table A1
Equation of State Parameters for Core Components

Components	T_0 (K)	V (cm ³ /mol)	α (10 ⁻⁵ K ⁻¹)	K_T (GPa)	K'_T	δ_T	q
Fe	1811	7.96	9.2	85.3	5.9	5.9	1.4
Fe—10 wt% S	1923	9.45	10.0	63.0	4.8	4.8 ^a	1.4 ^b

Note. Fe (Anderson & Ahrens, 1994) and Fe-10 wt% S (Balog et al., 2003). The thermal expansivity of Fe-10 wt% S is calculated from the volume and thermal expansivity of FeS (Kaiura & Toguri, 1979) at 1923K ($V = 12.603$ cm³/mol, $\alpha = 16.5 \times 10^{-5}$ K⁻¹) by applying equations (A1) and (A3).

^aSince δ_T is not available for Fe and Fe-10 wt% S, we made use of the following approximate relation (e.g., Poirier, 2000): $\delta_T \approx K'_T$. ^bTaken from Helffrich (2012).

compression at T_0 , we employ a third-order finite strain Birch-Murnaghan equation of state (Stixrude & Lithgow-Bertelloni, 2005a)

$$P = -3\epsilon(1 - 2\epsilon)^{\frac{5}{2}} \left[K_{T,0} - \frac{3}{2}K_{T,0} (K'_{T,0} - 4) \epsilon \right], \quad (\text{A7})$$

$$K_T = (1 - 2\epsilon)^{\frac{5}{2}} \left[K_{T,0} - K_{T,0} (3K'_{T,0} - 5) \epsilon + \frac{27}{2}K_{T,0} (K'_{T,0} - 4) \epsilon^2 \right], \quad (\text{A8})$$

$$K'_T = K'_{T,0} + \left[3K'^2_{T,0} - 21K'_{T,0} + \frac{143}{3} \right] \epsilon, \quad (\text{A9})$$

where $\epsilon = \frac{1}{2} \left(1 - \beta^{-\frac{2}{3}} \right)$ is the Eulerian strain, $\beta = V(P)/V_0$, volume, isothermal bulk modulus, and pressure derivative at (P, T_0) are denoted by $V(P)$, $K_T(P)$, and $K'_{T,0}(P)$, respectively, and zero-subscripted quantities are evaluated at reference conditions.

Volume at (P, T) is obtained from the definition of the thermal expansivity (e.g., Poirier, 2000):

$$V(P, T) = V(P) \exp \left[\alpha(P)(T - T_0) \right]. \quad (\text{A10})$$

The expression for $\alpha(P)$ follows from the definition of the Anderson-Grüneisen parameter δ_T (e.g., Poirier, 2000)

$$\alpha(P) = \alpha_0 \exp \left[-\frac{\delta_T}{q} (1 - \beta^q) \right], \quad (\text{A11})$$

where q is a material-dependent parameter. The temperature dependence of the isothermal bulk modulus K_T at pressure P can be derived from equations (A10) and (A11)

$$K_T(P, T) = \frac{K_T(P)}{1 + (T - T_0)\alpha(P)\delta_T\beta^q}. \quad (\text{A12})$$

Finally, we assume that $K'_T(P)$ is independent of temperature. The relevant material properties for the equations of state for Fe and FeS₁₀ are summarized in Table A1.

Appendix B: Geodynamical Simulations

Thermochemical compressible convection is studied using the code StagYY in a 2-D spherical annulus geometry (Hernlund & Tackley, 2008; Tackley, 2008). The equations of momentum, mass, and energy conservation are solved using a parallel direct solver (MUMPS) available in the PETSc package (Amestoy et al., 2000). We use the finite difference approximation on a staggered grid (Harlow & Welch, 1965) with a radially varying resolution (higher in the top and bottom boundary layers). The domain is discretized by 64×512 cells. Free slip boundary conditions are imposed on all domain boundaries. The surface temperature is fixed to 220 K, and the initial core temperature is 2500 K.

Lagrangian markers are advected through the mesh using second-order divergence-free spatial interpolation of the velocities and a fourth-order Runge-Kutta scheme. Each tracer carries several quantities such as composition, temperature, grain size, and radiogenic heating rate, among others. Numerical diffusion related to advection is limited by the use of tracers. Our petrological model considers solid and molten rocks as being a linear combination of basalt-eclogite (crustal material) and harzburgite (depleted mantle). The primordial

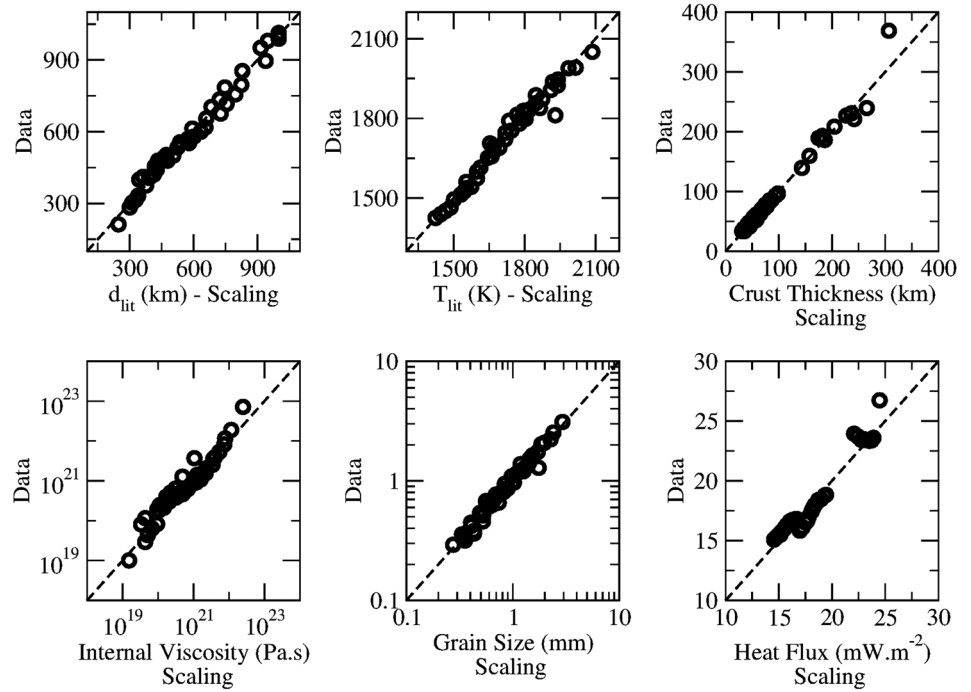


Figure B1. Present-day lithosphere thickness, lithosphere-asthenosphere boundary temperature, crustal thickness, internal viscosity (at 1,000 km depth), internal grain size, and surface heat flux after 4.5 Gyr of evolution, scaled using the approach described in section 6.2.

mantle starts with an initial petrological composition of 15% basalt (100% pyroxene-garnet) and 85% harzburgite (a mixture of 55% olivine and 45% pyroxene-garnet). For numerical efficiency the composition is stored and transported on tracers, while the evolution of the melt fraction is computed on the mesh field (which generates new molten tracers in each corresponding cell). A composition field is computed at cell centers by averaging of the tracers within the cell. The melt fraction is computed at every time step comparing the pressure-temperature conditions to a composition-dependent solidus function, considering a latent heat of 600 kJ/kg. In case melting occurs at less than ~600 km depth, molten tracers of fully basaltic composition are transported either to the top of the domain (eruption) or to the bottom of the crust (intrusion). The temperature of all erupted tracers is set to surface temperature, which tends to form a cold lithosphere. The temperature of intruded tracers (at the bottom of the crust) takes only adiabatic decompression into account, which tends to produce a warm lithosphere. The column of material between the melt source region and the intrusion or eruption location is moved downward to conserve mass. The solid residue left behind by the eruption-intrusion procedure is more harzburgitic than the initial solid. For more details regarding implementation the reader is referred to Nakagawa and Tackley (2004, 2012). The density in each cell is computed as the sum of pressure and thermal and compositional components, including solid-solid phase transitions. Olivine and pyroxene-garnet phases are treated separately, which enables accounting for the density increase associated with the basalt-eclogite phase transition.

Plastic yielding in the lithosphere is computed using a depth-dependent yield stress τ_y following Byerlee's law (Byerlee, 1978):

$$\tau_y = f \cdot P, \tag{B1}$$

where P is pressure and f is a friction coefficient (we chose $f = 0.35$ in the simulations here). The effective viscosity is computed from

$$\eta_{\text{eff}} = \min \left(\eta(P, T, d_{\text{grain}}), \frac{\tau_y}{2\dot{\epsilon}} \right), \tag{B2}$$

where $\dot{\epsilon}$ is the second invariant of the strain rate tensor. In the present study, viscosity depends neither on melt fraction nor on composition.

As we solve for compressible convection, adiabatic temperature, thermal conductivity, density, thermal expansivity, and heat capacity are all pressure dependent. We use a third-order Birch-Murnaghan equation of state which relates bulk modulus to pressure (see Tackley et al., 2013, for details). With each mineral phase is associated individual phase transition depths and physical properties so that solid olivine and pyroxene-garnet densities, for example, smoothly increase with depth but also contain discontinuities at the phase transitions (Rozel et al., 2017). Finally, melt density increases smoothly with pressure.

Acknowledgments

We thank Walter Kiefer and Ian Jackson for comments that helped improve the clarity of the manuscript. We also thank Michael Efroimsky for valuable comments on tidal deformation and additional suggestions for improving the manuscript. Finally, we thank Jeff Taylor and Gregor Golabek for helpful comments on an earlier version of this manuscript. A. K. and D. G. would like to acknowledge support from the Swiss National Science Foundation (SNF-ANR project 157133 "Seismology on Mars"). Computations were performed on the ETH cluster Euler. Models can be downloaded from <http://jupiter.ethz.ch/~akhan/amir/Models.html>.

References

- Agee, C. B., & Draper, D. S. (2004). Experimental constraints on the origin of Martian meteorites and the composition of the Martian mantle. *Earth and Planetary Science Letters*, 224, 415–429. <https://doi.org/10.1016/j.epsl.2004.05.022>
- Aместов, P. R., Duff, I. S., & l'Excellent, J.-Y. (2000). Multifrontal parallel distributed symmetric and unsymmetric solvers. *Computer Methods in Applied Mechanics and Engineering*, 184(2–4), 501–520.
- Anderson, W. W., & Ahrens, T. J. (1994). An equation of state for liquid iron and implications for the Earth's core. *Journal of Geophysical Research*, 99, 4273–4284. <https://doi.org/10.1029/93JB03158>
- Balmino, G., Duron, J., & Marty, J. (2005). A new Martian gravity field mean model and its time variations. AGU Fall Meeting Abstracts G53C.
- Balog, P. S., Secco, R. A., Rubie, D. C., & Frost, D. J. (2003). Equation of state of liquid Fe-10 wt% S: Implications for the metallic cores of planetary bodies. *Journal of Geophysical Research*, 108, 2124. <https://doi.org/10.1029/2001JB001646>
- Balta, J. B., & McSween, H. Y. (2013). Application of the MELTS algorithm to Martian compositions and implications for magma crystallization. *Journal of Geophysical Research: Planets*, 118, 2502–2519. <https://doi.org/10.1002/2013JE004461>
- Banerdt, W. B., Smrekar, S., Lognonné, P., Spohn, T., Asmar, S. W., Banfield, D., ... Hurst, K. (2013). InSight: A discovery mission to explore the interior of Mars. In *Lunar and Planetary Science Conference, Lunar and Planetary Institute Technical Report* (Vol. 44, p. 1915). Woodlands, TX.
- Baratoux, D., Samuel, H., Michaut, C., Toplis, M. J., Monnereau, M., Wiczcerek, M., ... Kurita, K. (2014). Petrological constraints on the density of the Martian crust. *Journal of Geophysical Research: Planets*, 119, 1707–1727. <https://doi.org/10.1002/2014JE004642>
- Baratoux, D., Toplis, M. J., Monnereau, M., & Gasnault, O. (2011). Thermal history of Mars inferred from orbital geochemistry of volcanic provinces. *Nature*, 475, 254. <https://doi.org/10.1038/nature10220>
- Bellis, C., & Holtzman, B. (2014). Sensitivity of seismic measurements to frequency-dependent attenuation and upper mantle structure: An initial approach. *Journal of Geophysical Research: Solid Earth*, 119, 5497–5517. <https://doi.org/10.1002/2013JB010831>
- Benjamin, D., Wahr, J., Ray, R. D., Egbert, G. D., & Desai, S. D. (2006). Constraints on mantle anelasticity from geodetic observations, and implications for the J_2 anomaly. *Geophysical Journal International*, 165, 3–16. <https://doi.org/10.1111/j.1365-246X.2006.02915.x>
- Bertka, C. M., & Fei, Y. (1997). Mineralogy of the Martian interior up to core-mantle boundary pressures. *Journal of Geophysical Research*, 102, 5251–5264. <https://doi.org/10.1029/96JB03270>
- Bertka, C. M., & Fei, Y. (1998). Density profile of an SNC model Martian interior and the moment-of-inertia factor of Mars. *Earth and Planetary Science Letters*, 157, 79–88. [https://doi.org/10.1016/S0012-821X\(98\)00030-2](https://doi.org/10.1016/S0012-821X(98)00030-2)
- Bertka, C. M., & Holloway, J. R. (1994). Anhydrous partial melting of an iron-rich mantle II: Primary melt compositions at 15 kbar. *Contributions to Mineralogy and Petrology*, 115, 323–338. <https://doi.org/10.1007/BF00310771>
- Bills, B. G., Neumann, G. A., Smith, D. E., & Zuber, M. T. (2005). Improved estimate of tidal dissipation within Mars from MOLA observations of the shadow of Phobos. *Journal of Geophysical Research*, 110, E07004. <https://doi.org/10.1029/2004JE002376>
- Birch, F. (1964). Density and composition of mantle and core. *Journal of Geophysical Research*, 69, 4377–4388. <https://doi.org/10.1029/JZ069i020p04377>
- Bogard, D. D., Clayton, R. N., Marti, K., Owen, T., & Turner, G. (2001). Martian volatiles: Isotopic composition, origin, and evolution. *Space Science Reviews*, 96, 425–458.
- Borg, L. E., & Draper, D. S. (2003). A petrogenic model for the origin and compositional variation of the Martian basaltic meteorites. *Meteoritics and Planetary Science*, 38, 1713–1731. <https://doi.org/10.1111/j.1945-5100.2003.tb00011.x>
- Böse, M., Clinton, J. F., Ceylan, S., Euchner, F., van Driel, M., Khan, A., ... Banerdt, W. B. (2017). A probabilistic framework for single-station location of seismicity on Earth and Mars. *Physics of the Earth and Planetary Interiors*, 262, 48–65. <https://doi.org/10.1016/j.pepi.2016.11.003>
- Bozdağ, E., Ruan, Y., Mettetz, N., Khan, A., Leng, K., van Driel, M., ... Banerdt, W. B. (2017). Simulations of seismic wave propagation on Mars. *Space Science Reviews*, 211, 571–594. <https://doi.org/10.1007/s11214-017-0350-z>
- Brankin, R. W., Gladwell, I., & Shampine, L. F. (1993). Rksuite: A suite of explicit Runge-Kutta codes. In *Contributions in Numerical Mathematics* (pp. 41–53). Singapore: World Scientific. Retrieved from http://www.worldscientific.com/doi/abs/10.1142/9789812798886_0004
- Breuer, D., & Moore, W. B. (2007). Dynamics and thermal history of the terrestrial planets, the Moon, and Io. In G. Schubert (Ed.), *Treatise on geophysics* (pp. 299–348). Amsterdam: Elsevier. <https://doi.org/10.1016/B978-044452748-6.00161-9>
- Breuer, D., Yuen, D. A., & Spohn, T. (1997). Phase transitions in the Martian mantle: Implications for partially layered convection. *Earth and Planetary Science Letters*, 148, 457–469. [https://doi.org/10.1016/S0012-821X\(97\)00049-6](https://doi.org/10.1016/S0012-821X(97)00049-6)
- Burbine, T. H., & O'Brien, K. M. (2004). Determining the possible building blocks of the Earth and Mars. *Meteoritics and Planetary Science*, 39, 667–681. <https://doi.org/10.1111/j.1945-5100.2004.tb00110.x>
- Byerlee, J. D. (1978). Friction of rocks. *Pure and Applied Geophysics*, 116, 615–626.
- Carr, M. H., & Head, J. W. (2010). Geologic history of Mars. *Earth and Planetary Science Letters*, 294, 185–203. <https://doi.org/10.1016/j.epsl.2009.06.042>
- Castillo-Rogez, J. C., & Banerdt, W. B. (2013). Impact of anelasticity on Mars' dissipative properties—Application to the InSight mission. In *Lunar and Planetary Science Conference* (Vol. 44, pp. 2679). Woodlands, TX.
- Ceylan, S., van Driel, M., Euchner, F., Khan, A., Clinton, J., Krischer, L., ... Giardini, D. (2017). From initial models of seismicity, structure, and noise to synthetic seismograms for Mars. *Space Science Reviews*, 211, 595–610. <https://doi.org/10.1007/s11214-017-0380-6>
- Clinton, J., Giardini, D., Lognonné, P., Banerdt, B., van Driel, M., Drilleau, M., ... Spiga, A. (2017). Preparing for InSight: An invitation to participate in a blind test for Martian seismicity. *Seismological Research Letters*, 88(5), 1290–1302. <https://doi.org/10.1785/0220170094>
- Collinet, M., Médard, E., Charlier, B., Vander Auwera, J., & Grove, T. L. (2015). Melting of the primitive Martian mantle at 0.5–2.2 GPa and the origin of basalts and alkaline rocks on Mars. *Earth and Planetary Science Letters*, 427, 83–94. <https://doi.org/10.1016/j.epsl.2015.06.056>
- Connolly, J. A. D. (2009). The geodynamic equation of state: What and how. *Geochemistry, Geophysics, Geosystems*, 10, Q10014. <https://doi.org/10.1029/2009GC002540>

- Connolly, J. A. D., & Khan, A. (2016). Uncertainty of mantle geophysical properties computed from phase equilibrium models. *Geophysical Research Letters*, *43*, 5026–5034. <https://doi.org/10.1002/2016GL068239>
- Dannberg, J., Eilon, Z., Faul, U., Gassmüller, R., Moulik, P., & Myhill, R. (2017). The importance of grain size to mantle dynamics and seismological observations. *Geochemistry, Geophysics, Geosystems*, *18*, 3034–3061. <https://doi.org/10.1002/2017GC006944>
- Drake, M. J., & Richter, K. (2002). Determining the composition of the Earth. *Nature*, *416*, 39–44. <https://doi.org/10.1038/416039a>
- Dreibus, G., & Wänke, H. (1984). Accretion of the Earth and inner planets. In *Geochemistry and Cosmochemistry* (pp. 3–11).
- Dreibus, G., & Wänke, H. (1985). Mars, a volatile-rich planet. *Meteoritics*, *20*, 367–381.
- Dreibus, G., & Wänke, H. (1987). Volatiles on Earth and Mars—A comparison. *Icarus*, *71*, 225–240. [https://doi.org/10.1016/0019-1035\(87\)90148-5](https://doi.org/10.1016/0019-1035(87)90148-5)
- Dumberry, M., & Rivoldini, A. (2015). Mercury's inner core size and core-crystallization regime. *Icarus*, *248*, 254–268. <https://doi.org/10.1016/j.icarus.2014.10.038>
- Efroimsky, M. (2012a). Tidal dissipation compared to seismic dissipation: In small bodies, earths, and super-earths. *Astrophysics Journal*, *746*, 150. <https://doi.org/10.1088/0004-637X/746/2/150>
- Efroimsky, M. (2012b). Bodily tides near spin-orbit resonances. *Celestial Mechanics and Dynamical Astronomy*, *112*(3), 283–330. <https://doi.org/10.1007/s10569-011-9397-4>
- Efroimsky, M. (2015). Tidal evolution of asteroidal binaries. Ruled by viscosity. Ignorant of rigidity. *Astrophysics Journal*, *150*, 98. <https://doi.org/10.1088/0004-6256/150/4/98>
- Efroimsky, M., & Lainey, V. (2007). Physics of bodily tides in terrestrial planets and the appropriate scales of dynamical evolution. *Journal of Geophysical Research*, *112*, E12003. <https://doi.org/10.1029/2007JE002908>
- Efroimsky, M., & Makarov, V. V. (2014). Tidal dissipation in a homogeneous spherical body. I. Methods. *The Astrophysical Journal*, *795*, 6. <https://doi.org/10.1088/0004-637X/795/1/6>
- Elkins-Tanton, L. T., Hess, P. C., & Parmentier, E. M. (2005). Possible formation of ancient crust on Mars through magma ocean processes. *Journal of Geophysical Research*, *110*, E12501. <https://doi.org/10.1029/2005JE002480>
- Elkins-Tanton, L. T., Parmentier, E. M., & Hess, P. C. (2003). Magma ocean fractional crystallization and cumulate overturn in terrestrial planets: Implications for Mars. *Meteoritics and Planetary Science*, *38*, 1753–1771. <https://doi.org/10.1111/j.1945-5100.2003.tb00013.x>
- Faul, U. H., Fitz Gerald, J. D., & Jackson, I. (2004). Shear wave attenuation and dispersion in melt-bearing olivine polycrystals: 2. Microstructural interpretation and seismological implications. *Journal of Geophysical Research*, *109*, B06202. <https://doi.org/10.1029/2003JB002407>
- Filiberto, J., Baratoux, D., Beaty, D., Breuer, D., Farcy, B. J., Grott, M., . . . Schwenzer, S. P. (2016). A review of volatiles in the Martian interior. *Meteoritics and Planetary Science*, *51*, 1935–1958. <https://doi.org/10.1111/maps.12680>
- Filiberto, J., & Dasgupta, R. (2015). Constraints on the depth and thermal vigor of melting in the Martian mantle. *Journal of Geophysical Research: Planets*, *120*, 109–122. <https://doi.org/10.1002/2014JE004745>
- Folkner, W. M., Asmar, S. W., Dehant, V., & Warwick, R. W. (2012). The Rotation and Interior Structure Experiment (RISE) for the InSight mission to Mars. In *Lunar and Planetary Science Conference* (Vol. 43, p. 1721). Woodlands, TX.
- Folkner, W. M., Yoder, C. F., Yuan, D. N., Standish, E. M., & Preston, R. A. (1997). Interior structure and seasonal mass redistribution of Mars from radio tracking of Mars Pathfinder. *Science*, *278*, 1749. <https://doi.org/10.1126/science.278.5344.1749>
- Genova, A., Goossens, S., Lemoine, F. G., Mazarico, E., Neumann, G. A., Smith, D. E., & Zuber, M. T. (2016). Seasonal and static gravity field of Mars from MGS, Mars Odyssey and MRO radio science. *Icarus*, *272*, 228–245. <https://doi.org/10.1016/j.icarus.2016.02.050>
- Goins, N. R., & Lazarewicz, A. R. (1979). Martian seismicity. *Geophysical Research Letters*, *6*, 368–370. <https://doi.org/10.1029/GL006i005p00368>
- Golabek, G. J., Keller, T., Gerya, T. V., Zhu, G., Tackley, P. J., & Connolly, J. A. D. (2011). Origin of the Martian dichotomy and tharsis from a giant impact causing massive magmatism. *Icarus*, *215*(1), 346–357. <https://doi.org/10.1016/j.icarus.2011.06.012>
- Golombek, M. P., Banerdt, W. B., Tanaka, K. L., & Tralli, D. M. (1992). A prediction of Mars seismicity from surface faulting. *Science*, *258*, 979–981. <https://doi.org/10.1126/science.258.5084.979>
- Grott, M., Baratoux, D., Hauber, E., Sautter, V., Mustard, J., Gasnault, O., . . . Toplis, M. J. (2013). Long-term evolution of the Martian crust-mantle system. *Space Science Reviews*, *174*, 49–111. <https://doi.org/10.1007/s11214-012-9948-3>
- Grott, M., & Breuer, D. (2008). The evolution of the Martian elastic lithosphere and implications for crustal and mantle rheology. *Icarus*, *193*, 503–515. <https://doi.org/10.1016/j.icarus.2007.08.015>
- Halliday, A. N., Wänke, H., Birck, J.-L., & Clayton, R. N. (2001). The accretion, composition and early differentiation of Mars. *Space Science Reviews*, *96*, 197–230.
- Harada, Y., Goossens, S., Matsumoto, K., Yan, J., Ping, J., Noda, H., & Haruyama, J. (2014). Strong tidal heating in an ultralow-viscosity zone at the core-mantle boundary of the Moon. *Nature Geoscience*, *7*, 569–572. <https://doi.org/10.1038/ngeo2211>
- Harder, H., & Christensen, U. R. (1996). A one-plume model of Martian mantle convection. *Nature*, *380*, 507–509. <https://doi.org/10.1038/380507a0>
- Harlow, F. H., & Welch, J. E. (1965). Numerical calculation of time-dependent viscous incompressible flow of fluid with a free surface. *Physics of Fluids*, *8*, 2182.
- Hart, S. R., & Dunn, T. (1993). Experimental cpx/melt partitioning of 24 trace elements. *Contributions to Mineralogy and Petrology*, *113*(1), 1–8. <https://doi.org/10.1007/BF00320827>
- Hauber, E., Grott, M., & Kronberg, P. (2010). Martian rifts: Structural geology and geophysics. *Earth and Planetary Science Letters*, *294*, 393–410. <https://doi.org/10.1016/j.epsl.2009.11.005>
- Hauk, S. A., Aurnou, J. M., & Dombard, A. J. (2006). Sulfur's impact on core evolution and magnetic field generation on Ganymede. *Journal of Geophysical Research*, *111*, E09008. <https://doi.org/10.1029/2005JE002557>
- Hauk, S. A., & Phillips, R. J. (2002). Thermal and crustal evolution of Mars. *Journal of Geophysical Research*, *107*, 5052. <https://doi.org/10.1029/2001JE001801>
- Hauri, E. H., Wagner, T. P., & Grove, T. L. (1994). Experimental and natural partitioning of Th, U, Pb and other trace elements between garnet, clinopyroxene and basaltic melts. *Chemical Geology*, *117*(1), 149–166. [https://doi.org/10.1016/0009-2541\(94\)90126-0](https://doi.org/10.1016/0009-2541(94)90126-0)
- Helfrich, G. (2012). How light element addition can lower core liquid wave speeds. *Geophysical Journal International*, *188*(3), 1065. <https://doi.org/10.1111/j.1365-246X.2011.05295.x>
- Helfrich, G. (2017). Mars core structure—Concise review and anticipated insights from InSight. *Progress in Earth and Planetary Science*, *4*(1), 24. <https://doi.org/10.1186/s40645-017-0139-4>
- Hernlund, J. W., & Tackley, P. J. (2008). Modeling mantle convection in the spherical annulus. *Physics of the Earth and Planetary Interiors*, *171*(1–4), 48–54. <https://doi.org/10.1016/j.pepi.2008.07.037>

- Hiraga, T., Tachibana, C., Ohashi, N., & Sano, S. (2010). Grain growth systematics for forsterite \pm enstatite aggregates: Effect of lithology on grain size in the upper mantle. *Earth and Planetary Science Letters*, 291(1–4), 10–20. <https://doi.org/10.1016/j.epsl.2009.12.026>
- Hirth, G., & Kohlstedt, D. (2013). Rheology of the upper mantle and the mantle wedge: A view from the experimentalists. In *Inside the subduction factory* (pp. 83–105). Washington, DC: American Geophysical Union. <https://doi.org/10.1029/138GM06>
- Hirth, G., & Kohlstedt, D. L. (1996). Water in the oceanic upper mantle: Implications for rheology, melt extraction and the evolution of the lithosphere. *Earth and Planetary Science Letters*, 144, 93–108. [https://doi.org/10.1016/0012-821X\(96\)00154-9](https://doi.org/10.1016/0012-821X(96)00154-9)
- Ivanov, M. A., & Head, J. W. (2013). The history of volcanism on Venus. *Planetary and Space Science*, 84, 66–92. <https://doi.org/10.1016/j.pss.2013.04.018>
- Jackson, I., & Faul, U. H. (2010). Grainsize-sensitive viscoelastic relaxation in olivine: Towards a robust laboratory-based model for seismological application. *Physics of the Earth and Planetary Interiors*, 183, 151–163. <https://doi.org/10.1016/j.pepi.2010.09.005>
- Jackson, I., Faul, U. H., & Skelton, R. (2014). Elastically accommodated grain-boundary sliding: New insights from experiment and modeling. *Physics of the Earth and Planetary Interiors*, 228, 203–210. <https://doi.org/10.1016/j.pepi.2013.11.014>
- Jackson, I., Fitz Gerald, J. D., Faul, U. H., & Tan, B. H. (2002). Grain-size-sensitive seismic wave attenuation in polycrystalline olivine. *Journal of Geophysical Research*, 107, 2360. <https://doi.org/10.1029/2001JB001225>
- Jacobson, R. A. (2010). The orbits and masses of the Martian satellites and the liberation of Phobos. *Astrophysics Journal*, 139, 668–679. <https://doi.org/10.1088/0004-6256/139/2/668>
- Kaiura, G. H., & Toguri, J. M. (1979). Densities of the molten FeS, FeS–Cu₂S and Fe–S–O systems—Utilizing a bottom-balance Archimedeian technique. *Canadian Metallurgical Quarterly*, 18(2), 155–164. <https://doi.org/10.1179/cm.1979.18.2.155>
- Karato, S. I. (2008). *Deformation of Earth materials*. Cambridge, UK: Cambridge University Press.
- Karato, S.-I. (2013). Geophysical constraints on the water content of the lunar mantle and its implications for the origin of the Moon. *Earth and Planetary Science Letters*, 384, 144–153. <https://doi.org/10.1016/j.epsl.2013.10.001>
- Karato, S.-I., & Jung, H. (1998). Water, partial melting and the origin of the seismic low velocity and high attenuation zone in the upper mantle. *Earth and Planetary Science Letters*, 157, 193–207. [https://doi.org/10.1016/S0012-821X\(98\)00034-X](https://doi.org/10.1016/S0012-821X(98)00034-X)
- Karato, S.-I., & Wu, P. (1993). Rheology of the upper mantle—A synthesis. *Science*, 260, 771–778. <https://doi.org/10.1126/science.260.5109.771>
- Keller, T., & Tackley, P. J. (2009). Towards self-consistent modeling of the Martian dichotomy: The influence of one-ridge convection on crustal thickness distribution. *Icarus*, 202(2), 429–443. Retrieved from <http://www.sciencedirect.com/science/article/B6WGF-4VXTSR1-2/2/000271ae%1b8140a0f820d927810982e6>
- Khan, A., & Connolly, J. A. D. (2008). Constraining the composition and thermal state of Mars from inversion of geophysical data. *Journal of Geophysical Research*, 113, E07003. <https://doi.org/10.1029/2007JE002996>
- Khan, A., Connolly, J. A. D., MacLennan, J., & Mosegaard, K. (2007). Joint inversion of seismic and gravity data for lunar composition and thermal state. *Geophysical Journal International*, 168, 243–258. <https://doi.org/10.1111/j.1365-246X.2006.03200.x>
- Khan, A., Connolly, J. A. D., Pommier, A., & Noir, J. (2014). Geophysical evidence for melt in the deep lunar interior and implications for lunar evolution. *Journal of Geophysical Research: Planets*, 119, 2197–2221. <https://doi.org/10.1002/2014JE004661>
- Khan, A., van Driel, M., Böse, M., Giardini, D., Ceylan, S., Yan, J., ... Banerdt, W. B. (2016). Single-station and single-event marsquake location and inversion for structure using synthetic Martian waveforms. *Physics of the Earth and Planetary Interiors*, 258, 28–42. <https://doi.org/10.1016/j.pepi.2016.05.017>
- Kiefer, W. S., Filiberto, J., Sandu, C., & Li, Q. (2015). The effects of mantle composition on the peridotite solidus: Implications for the magmatic history of Mars. *Geochimica et Cosmochimica Acta*, 162, 247–258. <https://doi.org/10.1016/j.gca.2015.02.010>
- Kiefer, W. S., & Li, Q. (2009). Mantle convection controls the observed lateral variations in lithospheric thickness on present-day Mars. *Geophysical Research Letters*, 36, L18203. <https://doi.org/10.1029/2009GL039827>
- Kiefer, W. S., & Li, Q. (2016). Water undersaturated mantle plume volcanism on present-day Mars. *Meteoritics and Planetary Science*, 51, 1993–2010. <https://doi.org/10.1111/maps.12720>
- Knapmeyer, M., Oberst, J., Hauber, E., Wählisch, M., Deuchler, C., & Wagner, R. (2006). Working models for spatial distribution and level of Mars' seismicity. *Journal of Geophysical Research*, 111, E11006. <https://doi.org/10.1029/2006JE002708>
- Konopliv, A. S., Asmar, S. W., Folkner, W. M., Karatekin, Ö., Nunes, D. C., Smrekar, S. E., ... Zuber, M. T. (2011). Mars high resolution gravity fields from MRO, Mars seasonal gravity, and other dynamical parameters. *Icarus*, 211, 401–428. <https://doi.org/10.1016/j.icarus.2010.10.004>
- Konopliv, A. S., Park, R. S., & Folkner, W. M. (2016). An improved JPL Mars gravity field and orientation from Mars orbiter and lander tracking data. *Icarus*, 274, 253–260. <https://doi.org/10.1016/j.icarus.2016.02.052>
- Konopliv, A. S., Yoder, C. F., Standish, E. M., Yuan, D.-N., & Sjogren, W. L. (2006). A global solution for the Mars static and seasonal gravity, Mars orientation, Phobos and Deimos masses, and Mars ephemeris. *Icarus*, 182, 23–50. <https://doi.org/10.1016/j.icarus.2005.12.025>
- Kuskov, O. L., & Panferov, A. B. (1993). Thermodynamic models for the structure of the Martian upper mantle. *Geochemistry International*, 30, 132. <https://doi.org/10.1051/0004-6361:20065466>
- Lambeck, K. (1979). On the orbital evolution of the Martian satellites. *Journal of Geophysical Research*, 84, 5651–5658. <https://doi.org/10.1029/JB084iB10p05651>
- Larmat, C., Montagner, J.-P., Capdeville, Y., Banerdt, W. B., Lognonné, P., & Vilotte, J.-P. (2008). Numerical assessment of the effects of topography and crustal thickness on Martian seismograms using a coupled modal solution spectral element method. *Icarus*, 196, 78–89. <https://doi.org/10.1016/j.icarus.2007.12.030>
- Lawrence, J. F., & Shearer, P. M. (2006). Constraining seismic velocity and density for the mantle transition zone with reflected and transmitted waveforms. *Geochemistry, Geophysics, Geosystems*, 7, Q10012. <https://doi.org/10.1029/2006GC001339>
- Li, Q., & Kiefer, W. S. (2007). Mantle convection and magma production on present-day Mars: Effects of temperature-dependent rheology. *Geophysical Research Letters*, 34, L16203. <https://doi.org/10.1029/2007GL030544>
- Lodders, K., & Fegley, B. (1997). An oxygen isotope model for the composition of Mars. *Icarus*, 126, 373–394. <https://doi.org/10.1006/icar.1996.5653>
- Lognonné, P., Banerdt, W. B., Giardini, D., Christensen, U., Mimoun, D., de Raucourt, S., ... Tromp, J. (2012). InSight and single-station broadband seismology: From signal and noise to interior structure determination. In *Lunar and Planetary Science Conference, Lunar and Planetary Institute Technical Report* (Vol. 43, p. 1983).
- Lognonné, P., Beyneix, J. G., Banerdt, W. B., Cacho, S., Karczewski, J. F., & Morand, M. (1996). Ultra broad band seismology on InterMarsNet. *Planets and Space Science*, 44, 1237. [https://doi.org/10.1016/S0032-0633\(96\)00083-9](https://doi.org/10.1016/S0032-0633(96)00083-9)
- Lognonné, P., & Mosser, B. (1993). Planetary seismology. *Surveys in Geophysics*, 14, 239–302. <https://doi.org/10.1007/BF00690946>

- Longhi, J., Knittle, E., Holloway, J. R., & Wänke, H. (1992). The bulk composition, mineralogy and internal structure of Mars. In H. H. Kieffer, B. M. Jakosky, C. W. Snyder, & M. S. Matthews (Eds.), *Mars* (pp. 184–208). Tucson: University of Arizona Press.
- Maaløe, S. (2004). The solidus of harzburgite to 3 gPa pressure: The compositions of primary abyssal tholeiite. *Mineralogy and Petrology*, 81(1), 1–17. <https://doi.org/10.1007/s00710-004-0028-6>
- Marinova, M. M., Aharonson, O., & Asphaug, E. (2008). Mega-impact formation of the Mars hemispheric dichotomy. *Nature*, 453, 1216–1219. <https://doi.org/10.1038/nature07070>
- Marty, J. C., Balmino, G., Duron, J., Rosenblatt, P., Le Maistre, S., Rivoldini, A., . . . Van Hoolst, T. (2009). Martian gravity field model and its time variations from MGS and Odyssey data. *Planetary and Space Science*, 57, 350–363. <https://doi.org/10.1016/j.pss.2009.01.004>
- Matsukage, K. N., Nagayo, Y., Whitaker, M. L., Takahashi, E., & Kawasaki, T. (2013). Melting of the Martian mantle from 1.0 to 4.5 GPa. *Journal of Mineralogical and Petrological Sciences*, 108(4), 201–214. <https://doi.org/10.2465/jmps.120820>
- McCarthy, C., & Takei, Y. (2011). Anelasticity and viscosity of partially molten rock analogue: Toward seismic detection of small quantities of melt. *Geophysical Research Letters*, 38, L18306. <https://doi.org/10.1029/2011GL048776>
- McCarthy, C., Takei, Y., & Hiraga, T. (2011). Experimental study of attenuation and dispersion over a broad frequency range: 2. The universal scaling of polycrystalline materials. *Journal of Geophysical Research*, 116, B09207. <https://doi.org/10.1029/2011JB008384>
- McCubbin, F. M., Hauri, E. H., Elardo, S. M., Vander Kaaden, K. E., Wang, J., & Shearer, C. K. (2012). Hydrous melting of the Martian mantle produced both depleted and enriched shergottites. *Geology*, 40(8), 683–686. <http://geology.gsapubs.org/content/40/8/683.abstract>
- McSween, H. Y. (1985). SNC meteorites—Clues to Martian petrologic evolution? *Reviews of Geophysics*, 23, 391–416. <https://doi.org/10.1029/RG023i004p00391>
- McSween, H. Y. (1994). What we have learned about Mars from SNC meteorites. *Meteoritics*, 29, 757–779.
- McSween, H. Y. Jr., & McLennan, S. M. (2014). Mars. In K. Turekian, H. Holland, & A. M. Davis (Eds.), *Planets, Asteroids, Comets and The Solar System, Treatise on Geochemistry* (2nd ed., Vol. 2, pp. 251–300). Amsterdam: Elsevier. <https://doi.org/10.1016/B978-0-08-095975-7.00125-X>
- Mei, S., & Kohlstedt, D. L. (2000). Influence of water on plastic deformation of olivine aggregates: 2. Dislocation creep regime. *Journal of Geophysical Research*, 105, 21,471–21,481. <https://doi.org/10.1029/2000JB900180>
- Minster, J. B., & Anderson, D. L. (1981). A model of dislocation-controlled rheology for the mantle. *The Royal Society*, 299(1449), 319–356. <https://doi.org/10.1098/rsta.1981.0025>
- Mocquet, A., Rosenblatt, P., Dehant, V., & Verhoeven, O. (2011). The deep interior of Venus, Mars, and the Earth: A brief review and the need for planetary surface-based measurements. *Planetary and Space Science*, 59(10), 1048–1061. <https://doi.org/10.1016/j.pss.2010.02.002>
- Mocquet, A., Vacher, P., Grasset, O., & Sotin, C. (1996). Theoretical seismic models of Mars: The importance of the iron content of the mantle. *Planets and Space Science*, 44, 1251–1268. [https://doi.org/10.1016/S0032-0633\(96\)00086-4](https://doi.org/10.1016/S0032-0633(96)00086-4)
- Mohapatra, R. K., & Murty, S. V. S. (2003). Precursors of Mars—Constraints from nitrogen and oxygen isotopic compositions of Martian meteorites. *Meteoritics and Planetary Science*, 38, 225–242. <https://doi.org/10.1111/j.1945-5100.2003.tb00261.x>
- Morgan, J. W., & Anders, E. (1979). Chemical composition of Mars. *Geochimica et Cosmochimica Acta*, 43, 1601–1610.
- Morschhauser, A., Grott, M., & Breuer, D. (2011). Crustal recycling, mantle dehydration, and the thermal evolution of Mars. *Icarus*, 212, 541–558. <https://doi.org/10.1016/j.icarus.2010.12.028>
- Mosegaard, K., & Tarantola, A. (1995). Monte Carlo sampling of solutions to inverse problems. *Journal of Geophysical Research*, 100(B7), 12,431–12,447.
- Nakagawa, T., & Tackley, P. J. (2012). Influence of magmatism on mantle cooling, surface heat flow and Urey ratio. *Earth and Planetary Science Letters*, 329–330, 1–10. <https://doi.org/10.1016/j.epsl.2012.02.011>
- Nakagawa, T., & Tackley, P. J. (2004). Effects of thermo-chemical mantle convection on the thermal evolution of the Earth's core. *Earth and Planetary Science Letters*, 220(1), 107–119.
- Nakagawa, T., & Tackley, P. J. (2005). Deep mantle heat flow and thermal evolution of the Earth's core in thermochemical multiphase models of mantle convection. *Geochemistry, Geophysics, Geosystems*, 6, Q08003. <https://doi.org/10.1029/2005GC000967>
- Nakamura, Y. (1977). Seismic energy transmission in an intensively scattering environment. *Journal of Geophysics Zeitschrift Geophysik*, 43, 389–399.
- Neukum, G., Jaumann, R., Hoffmann, H., Hauber, E., Head, J. W., Basilevsky, A. T., . . . HRSC Co-Investigator Team (2004). Recent and episodic volcanic and glacial activity on Mars revealed by the High Resolution Stereo Camera. *Nature*, 432, 971–979. <https://doi.org/10.1038/nature03231>
- Neumann, G. A., Zuber, M. T., Wieczorek, M. A., McGovern, P. J., Lemoine, F. G., & Smith, D. E. (2004). Crustal structure of Mars from gravity and topography. *Journal of Geophysical Research*, 109, E08002. <https://doi.org/10.1029/2004JE002262>
- Niles, P. B., Boynton, W. V., Hoffman, J. H., Ming, D. W., & Hamara, D. (2010). Stable isotope measurements of Martian atmospheric CO₂ at the Phoenix landing site. *Science*, 329, 1334–1337. <https://doi.org/10.1126/science.1192863>
- Nimmo, F., & Faul, U. H. (2013). Dissipation at tidal and seismic frequencies in a melt-free, anhydrous Mars. *Journal of Geophysical Research: Planets*, 118, 2558–2569. <https://doi.org/10.1002/2013JE004499>
- Nimmo, F., Faul, U. H., & Garnero, E. J. (2012). Dissipation at tidal and seismic frequencies in a melt-free Moon. *Journal of Geophysical Research*, 117, E09005. <https://doi.org/10.1029/2012JE004160>
- Nimmo, F., Hart, S. D., Korycansky, D. G., & Agnor, C. B. (2008). Implications of an impact origin for the Martian hemispheric dichotomy. *Nature*, 453, 1220–1223. <https://doi.org/10.1038/nature07025>
- Norman, M. D. (1999). The composition and thickness of the crust of Mars estimated from REE and Nd isotopic compositions of Martian meteorites. *Meteoritics and Planetary Science*, 34, 439–449. <https://doi.org/10.1111/j.1945-5100.1999.tb01352.x>
- Ogawa, M., & Yanagisawa, T. (2012). Two-dimensional numerical studies on the effects of water on Martian mantle evolution induced by magmatism and solid-state mantle convection. *Journal of Geophysical Research*, 117, E06004. <https://doi.org/10.1029/2012JE004054>
- Okal, E. A., & Anderson, D. L. (1978). Theoretical models for Mars and their seismic properties. *Icarus*, 33, 514–528. [https://doi.org/10.1016/0019-1035\(78\)90187-2](https://doi.org/10.1016/0019-1035(78)90187-2)
- Palme, H., & O'Neill, H. S. C. (2003). Cosmochemical estimates of mantle composition. *Treatise on Geochemistry*, 2, 568. <https://doi.org/10.1016/B0-08-043751-6/02177-0>
- Panning, M. P., Lognonné, P., Bruce Banerdt, W., Garcia, R., Golombek, M., Kedar, S., . . . Wookey, J. (2016). Planned products of the Mars structure service for the InSight mission to Mars. *Space Science Reviews*, 211, 611–650. <https://doi.org/10.1007/s11214-016-0317-5>
- Phillips, R. J., Zuber, M. T., Solomon, S. C., Golombek, M. P., Jakosky, B. M., Banerdt, W. B., . . . Hauck, S. A. (2001). Ancient geodynamics and global-scale hydrology on Mars. *Science*, 291, 2587–2591. <https://doi.org/10.1126/science.1058701>
- Plesa, A.-C., Grott, M., Tosi, N., Breuer, D., Spohn, T., & Wieczorek, M. A. (2016). How large are present-day heat flux variations across the surface of Mars? *Journal of Geophysical Research: Planets*, 121, 2386–2403. <https://doi.org/10.1002/2016JE005126>

- Plesa, A.-C., Tosi, N., Grott, M., & Breuer, D. (2015). Thermal evolution and Urey ratio of Mars. *Journal of Geophysical Research: Planets*, *120*, 995–1010. <https://doi.org/10.1002/2014JE004748>
- Poirier, J. P. (2000). *Introduction to physics of the Earth*. Cambridge, UK: Cambridge University Press.
- Pommier, A., Grove, T. L., & Charlier, B. (2012). Water storage and early hydrous melting of the Martian mantle. *Earth and Planetary Science Letters*, *333*, 272–281. <https://doi.org/10.1016/j.epsl.2012.03.030>
- Rai, N., & Westrenen, W. (2013). Core-mantle differentiation in Mars. *Journal of Geophysical Research: Planets*, *118*, 1195–1203. <https://doi.org/10.1002/jgre.20093>
- Ray, R. D., Eanes, R. J., & Lemoine, F. G. (2001). Constraints on energy dissipation in the Earth's body tide from satellite tracking and altimetry. *Geophysical Journal International*, *144*, 471–480. <https://doi.org/10.1046/j.1365-246X.2001.00356.x>
- Reese, C. C., Orth, C. P., & Solomatov, V. S. (2010). Impact origin for the Martian crustal dichotomy: Half emptied or half filled? *Journal of Geophysical Research*, *115*, E05004. <https://doi.org/10.1029/2009JE003506>
- Righter, K., Drake, M. J., & Scott, E. R. D. (2006). Compositional relationships between meteorites and terrestrial planets. In D. S. Lauretta & H. Y. McSween Jr. (Eds.), *Meteorites and the early solar system II* (Vol. 943, pp. 803–828). Tucson: University of Arizona Press.
- Ringwood, A. E. (1979). *Origin of the Earth and Moon* (p. 307). New York: Springer-Verlag New York, Inc.
- Rivoldini, A., Van Hoolst, T., Verhoeven, O., Mocquet, A., & Dehant, V. (2011). Geodesy constraints on the interior structure and composition of Mars. *Icarus*, *213*, 451–472. <https://doi.org/10.1016/j.icarus.2011.03.024>
- Roberts, J. H., & Nimmo, F. (2008). Tidal heating and the long-term stability of a subsurface ocean on Enceladus. *Icarus*, *194*, 675–689. <https://doi.org/10.1016/j.icarus.2007.11.010>
- Roberts, J. H., & Zhong, S. (2006). Degree-1 convection in the Martian mantle and the origin of the hemispheric dichotomy. *Journal of Geophysical Research*, *111*, E06013. <https://doi.org/10.1029/2005JE002668>
- Roosbeek, F. (1999). Analytical developments of rigid Mars nutation and tide generating potential series. *Celestial Mechanics and Dynamical Astronomy*, *75*(4), 287–300. <http://doi.org/10.1023/A:1008310918697>
- Rozel, A. B., Golabek, G. J., Jain, C., Tackley, P. J., & Gerya, T. (2017). Continental crust formation on early Earth controlled by intrusive magmatism. *Nature*, *545*, 332–335. <https://doi.org/10.1038/nature22042>
- Ruedas, T., Tackley, P. J., & Solomon, S. C. (2013a). Thermal and compositional evolution of the Martian mantle: Effects of phase transitions and melting. *Physics of the Earth and Planetary Interiors*, *216*, 32–58.
- Ruedas, T., Tackley, P. J., & Solomon, S. C. (2013b). Thermal and compositional evolution of the Martian mantle: Effects of water. *Physics of the Earth and Planetary Interiors*, *220*, 50–72. <https://doi.org/10.1016/j.pepi.2012.12.002>
- Sanloup, C., Jambon, A., & Gillet, P. (1999). A simple chondritic model of Mars. *Physics of the Earth and Planetary Interiors*, *112*, 43–54. [https://doi.org/10.1016/S0031-9201\(98\)00175-7](https://doi.org/10.1016/S0031-9201(98)00175-7)
- Seidelmann, P. K., Abalakin, V. K., Bursa, M., Davies, M. E., de Bergh, C., Lieske, J. H., ... Thomas, P. C. (2002). Report of the IAU/IAG working group on cartographic coordinates and rotational elements of the planets and satellites: 2000. *Celestial Mechanics and Dynamical Astronomy*, *82*(1), 83–111. <https://doi.org/10.1023/A:1013939327465>
- Smith, J. C., & Born, G. H. (1976). Secular acceleration of PHOBOS and Q of Mars. *Icarus*, *27*, 51–53. [https://doi.org/10.1016/0019-1035\(76\)90183-4](https://doi.org/10.1016/0019-1035(76)90183-4)
- Sohl, F., Schubert, G., & Spohn, T. (2005). Geophysical constraints on the composition and structure of the Martian interior. *Journal of Geophysical Research*, *110*, E12008. <https://doi.org/10.1029/2005JE002520>
- Sohl, F., & Spohn, T. (1997). The interior structure of Mars: Implications from SNC meteorites. *Journal of Geophysical Research*, *102*, 1613–1636.
- Solomatov, V. S. (2001). Grain size-dependent viscosity convection and the thermal evolution of the Earth. *Earth and Planetary Science Letters*, *191*, 203–212. [https://doi.org/10.1016/S0012-821X\(01\)00426-5](https://doi.org/10.1016/S0012-821X(01)00426-5)
- Solomatov, V. S., & Reese, C. C. (2008). Grain size variations in the Earth's mantle and the evolution of primordial chemical heterogeneities. *Journal of Geophysical Research*, *113*, B07408. <https://doi.org/10.1029/2007JB005319>
- Solomon, S. C., Aharonson, O., Aurnou, J. M., Banerdt, W. B., Carr, M. H., Dombard, A. J., ... Zuber, M. T. (2005). New perspectives on ancient Mars. *Science*, *307*(5713), 1214–1220. <https://doi.org/10.1126/science.1101812>
- Solomon, S. C., Anderson, D. L., Banerdt, W. B., Butler, R. G., Davis, P. M., Duennebieber, F. K., ... Phillips, R. J. (1991). Scientific rationale and requirements for a global seismic network on Mars. Report of a workshop (pp. 57).
- Spohn, T., Grott, M., Smrekar, S., Krause, C., Hudson, T. L., & HP3 Instrument Team (2014). Measuring the Martian heat flow using the heat flow and physical properties package (HP3). In *Lunar and Planetary Science Conference* (Vol. 45, pp. 1916). Woodlands, TX.
- Stähler, S. C., Sigloch, K., & Nissen-Meyer, T. (2012). Triplicated *P*-wave measurements for waveform tomography of the mantle transition zone. *Solid Earth*, *3*(2), 339–354. <https://doi.org/10.5194/se-3-339-2012>
- Stevenson, D. J. (2001). Mars' core and magnetism. *Nature*, *412*, 214–219.
- Stewart, A. J., Schmidt, M. W., van Westrenen, W., & Liebske, C. (2007). Mars: A new core-crystallization regime. *Science*, *316*, 1323–5. <https://doi.org/10.1126/science.1140549>
- Stixrude, L., & Lithgow-Bertelloni, C. (2005a). Thermodynamics of mantle minerals—I. Physical properties. *Geophysical Journal International*, *162*, 610–632. <https://doi.org/10.1111/j.1365-246X.2005.02642.x>
- Stixrude, L., & Lithgow-Bertelloni, C. (2005b). Mineralogy and elasticity of the oceanic upper mantle: Origin of the low-velocity zone. *Journal of Geophysical Research*, *110*, B03204. <https://doi.org/10.1029/2004JB002965>
- Stixrude, L., & Lithgow-Bertelloni, C. (2011). Thermodynamics of mantle minerals—II. Phase equilibria. *Geophysical Journal International*, *184*, 1180–1213. <https://doi.org/10.1111/j.1365-246X.2010.04890.x>
- Stolper, E., & McSween, H. Y. (1979). Petrology and origin of the shergottite meteorites. *Geochimica et Cosmochimica Acta*, *43*, 1475–1477. [https://doi.org/10.1016/0016-7037\(79\)90142-X](https://doi.org/10.1016/0016-7037(79)90142-X)
- Surkov, Y. A. (1977). *Gamma spectrometry in cosmic investigations*. Moscow: Atomizdat.
- Tackley, P. J. (2008). Modelling compressible mantle convection with large viscosity contrasts in a three-dimensional spherical shell using the yin-yang grid. *Physics of the Earth and Planetary Interiors*, *171*, 7–18. <https://doi.org/10.1016/j.pepi.2008.08.005>
- Tackley, P. J., Ammann, M., Brodholt, J. P., Dobson, D. P., & Valencia, D. (2013). Mantle dynamics in super-Earths: Post-perovskite rheology and self-regulation of viscosity. *Icarus*, *225*, 50–61.
- Takei, Y. (2017). Effects of partial melting on seismic velocity and attenuation: A new insight from experiments. *Annual Review of Earth and Planetary Sciences*, *45*(1), 447–470. Retrieved from <http://www.annualreviews.org/doi/abs/10.1146/annurev-earth-063016-01582%0>
- Takei, Y., Karasawa, F., & Yamauchi, H. (2014). Temperature, grain size, and chemical controls on polycrystal anelasticity over a broad frequency range extending into the seismic range. *Journal of Geophysical Research: Solid Earth*, *119*, 5414–5443. <https://doi.org/10.1002/2014JB011146>

- Tauzin, B., Debayle, E., & Wittlinger, G. (2008). The mantle transition zone as seen by global PDS phases: No clear evidence for a thin transition zone beneath hotspots. *Journal of Geophysical Research*, *113*, B08309. <https://doi.org/10.1029/2007JB005364>
- Taylor, G. J. (2013). The bulk composition of Mars. *Chemie der Erde/Geochemistry*, *73*, 401–420. <https://doi.org/10.1016/j.chemer.2013.09.006>
- Taylor, S. R. (1980). Refractory and moderately volatile element abundances in the Earth, Moon and meteorites. In S. A. Bedini (Ed.), *Lunar and Planetary Science Conference Proceedings* (Vol. 11, pp. 333–348). Woodlands, TX.
- Taylor, S. R. (1999). The Leonard Award address: On the difficulties of making Earth-like planets. *Meteoritics and Planetary Science*, *34*, 317–329. <https://doi.org/10.1111/j.1945-5100.1999.tb01342.x>
- Taylor, S. R., & McLennan, S. M. (2009). *Planetary Crusts: Their Composition, Origin, and Evolution* (378 pp.). Cambridge: Cambridge University Press.
- Taylor, S. R., Taylor, G. J., & Taylor, L. A. (2006). The Moon: A Taylor perspective. *Geochimica et Cosmochimica Acta*, *70*, 5904–5918. <https://doi.org/10.1016/j.gca.2006.06.262>
- Teauby, N. A., & Wookey, J. (2011). Seismic detection of meteorite impacts on Mars. *Physics of the Earth and Planetary Interiors*, *186*, 70–80. <https://doi.org/10.1016/j.pepi.2011.03.004>
- Šrámek, O., & Zhong, S. (2010). Long-wavelength stagnant lid convection with hemispheric variation in lithospheric thickness: Link between Martian crustal dichotomy and Tharsis? *Journal of Geophysical Research*, *115*, E09010. <https://doi.org/10.1029/2010JE003597>
- van Hoolst, T., Dehant, V., Folkner, W., Asmar, S., Rivoldini, A., & Banerdt, W. B. (2012). Interior of Mars from geodesy. In *Lunar and Planetary Science Conference* (Vol. 43, pp. 2157). Woodlands, TX.
- Van Hoolst, T., Dehant, V., Roosbeek, F., & Lognonné, P. (2003). Tidally induced surface displacements, external potential variations, and gravity variations on Mars. *Icarus*, *161*, 281–296. [https://doi.org/10.1016/S0019-1035\(02\)00045-3](https://doi.org/10.1016/S0019-1035(02)00045-3)
- van Thienen, P., Rivoldini, A., Van Hoolst, T., & Lognonné, P. (2006). A top-down origin for Martian mantle plumes. *Icarus*, *185*, 197–210. <https://doi.org/10.1016/j.icarus.2006.06.008>
- Verhoeven, O., Rivoldini, A., Vacher, P., Mocquet, A., Choblet, G., Menvielle, M., ... Lognonné, P. (2005). Interior structure of terrestrial planets: Modeling Mars' mantle and its electromagnetic, geodetic, and seismic properties. *Journal of Geophysical Research*, *110*, E04009. <https://doi.org/10.1029/2004JE002271>
- Wang, Y., Wen, L., & Weidner, D. J. (2013). Composition of Mars constrained using geophysical observations and mineral physics modeling. *Physics of the Earth and Planetary Interiors*, *224*, 68–76. <https://doi.org/10.1016/j.pepi.2013.08.005>
- Wänke, H., & Dreibus, G. (1994). Chemistry and accretion history of Mars. *Philosophical Transactions of the Royal Society of London Series A*, *349*, 285–293. <https://doi.org/10.1098/rsta.1994.0132>
- Wasson, J. T., & Kallemeyn, G. W. (1988). Compositions of chondrites. *Philosophical Transactions of the Royal Society of London Series A*, *325*, 535–544. <https://doi.org/10.1098/rsta.1988.0066>
- Weber, R. C., Lin, P.-Y., Garnero, E. J., Williams, Q., & Lognonné, P. (2011). Seismic detection of the lunar core. *Science*, *331*, 309–. <https://doi.org/10.1126/science.1199375>
- Werner, S. C. (2009). The global Martian volcanic evolutionary history. *Icarus*, *201*, 44–68. <https://doi.org/10.1016/j.icarus.2008.12.019>
- Wieczorek, M. A., & Zuber, M. T. (2004). Thickness of the Martian crust: Improved constraints from geoid-to-topography ratios. *Journal of Geophysical Research*, *109*, E01009. <https://doi.org/10.1029/2003JE002153>
- Williams, J. G., & Boggs, D. H. (2015). Tides on the Moon: Theory and determination of dissipation. *Journal of Geophysical Research: Planets*, *120*, 689–724. <https://doi.org/10.1002/2014JE004755>
- Williams, J. G., Boggs, D. H., Yoder, C. F., Ratcliff, J. T., & Dickey, J. O. (2001). Lunar rotational dissipation in solid body and molten core. *Journal of Geophysical Research*, *106*, 27,933–27,968. <https://doi.org/10.1029/2000JE001396>
- Williams, J. G., Konopliv, A. S., Boggs, D. H., Park, R. S., Yuan, D.-N., Lemoine, F. G., ... Zuber, M. T. (2014). Lunar interior properties from the GRAIL mission. *Journal of Geophysical Research: Planets*, *119*, 1546–1578. <https://doi.org/10.1002/2013JE004559>
- Williams, J.-P., & Nimmo, F. (2004). Thermal evolution of the Martian core: Implications for an early dynamo. *Geology*, *32*, 97–100. <https://doi.org/10.1130/G19975.1>
- Wood, B. J., & Holloway, J. R. (1984). A thermodynamic model for subsolidus equilibria in the system CaO-MgO-Al₂O₃-SiO₂. *Geochimica et Cosmochimica Acta*, *48*, 159–176. [https://doi.org/10.1016/0016-7037\(84\)90358-2](https://doi.org/10.1016/0016-7037(84)90358-2)
- Xie, S., & Tackley, P. J. (2004). Evolution of helium and argon isotopes in a convecting mantle. *Physics of the Earth and Planetary Interiors*, *146*, 417–439. <https://doi.org/10.1016/j.pepi.2004.04.003>
- Yamazaki, D., Inoue, T., Okamoto, M., & Irifune, T. (2005). Grain growth kinetics of ringwoodite and its implication for rheology of the subducting slab. *Earth and Planetary Science Letters*, *236*, 871–881. <https://doi.org/10.1016/j.epsl.2005.06.005>
- Yoder, C. F. (1982). Tidal rigidity of PHOBOS. *Icarus*, *49*, 327–346. [https://doi.org/10.1016/0019-1035\(82\)90040-9](https://doi.org/10.1016/0019-1035(82)90040-9)
- Yoder, C. F. (1995). Astrometric and geodetic properties of Earth and the solar system. In T. J. Ahrens (Ed.), *Global Earth physics: A handbook of physical constants, AGU reference shelf Series* (Vol. 1, pp. 1–31). Washington, DC: American Geophysical Union.
- Yoder, C. F., Konopliv, A. S., Yuan, D. N., Standish, E. M., & Folkner, W. M. (2003). Fluid core size of Mars from detection of the solar tide. *Science*, *300*, 299–303. <https://doi.org/10.1126/science.1079645>
- Zhao, Y.-H., Zimmerman, M. E., & Kohlstedt, D. L. (2009). Effect of iron content on the creep behavior of olivine: 1. Anhydrous conditions. *Earth and Planetary Science Letters*, *287*(1–2), 229–240. Retrieved from <http://www.sciencedirect.com/science/article/pii/S0012821X09004683>
- Zharkov, V. N., & Gudkova, T. V. (1997). On the dissipative factor of the Martian interiors. *Planets and Space Science*, *45*, 401–407. [https://doi.org/10.1016/S0032-0633\(96\)00144-4](https://doi.org/10.1016/S0032-0633(96)00144-4)
- Zharkov, V. N., & Gudkova, T. V. (2005). Construction of Martian Interior Model. *Solar System Research*, *39*, 343–373. <https://doi.org/10.1007/s11208-005-0049-7>
- Zharkov, V. N., & Gudkova, T. V. (2009). The period and Q of the Chandler wobble of Mars. *Planetary and Space Science*, *57*, 288–295. <https://doi.org/10.1016/j.pss.2008.11.010>
- Zharkov, V. N., & Gudkova, T. V. (2014). Seismic model of Mars: Effects of hydration. *Planetary and Space Science*, *104*, 270–278. <https://doi.org/10.1016/j.pss.2014.10.009>
- Zharkov, V. N., Gudkova, T. V., & Batov, A. V. (2017). On Estimating the Dissipative Factor of the Martian Interior. *Solar System Research*, *51*, 479–490. <https://doi.org/10.1134/S0038094617060089>
- Zheng, Y., Nimmo, F., & Lay, T. (2015). Seismological implications of a lithospheric low seismic velocity zone in Mars. *Physics of the Earth and Planetary Interiors*, *240*, 132–141. <https://doi.org/10.1016/j.pepi.2014.10.004>
- Zhong, S. (2009). Migration of Tharsis volcanism on Mars caused by differential rotation of the lithosphere. *Nature Geoscience*, *2*, 19–23. <https://doi.org/10.1038/ngeo392>
- Zhong, S., & Zuber, M. T. (2001). Degree-1 mantle convection and the crustal dichotomy on Mars. *Earth and Planetary Science Letters*, *190*, 75–84.